

Spectral Wave Explicit Navier-Stokes Equations for wave-structure interactions using two-phase Computational Fluid Dynamics solvers

Zhaobin LI¹, Benjamin Bouscasse*¹, Guillaume Ducrozet¹, Lionel Gentaz¹, David Le Touzé¹, and Pierre Ferrant¹

¹École Centrale Nantes, LHEEA Lab. (ECN and CNRS), Nantes, France

Abstract

This paper proposes an efficient potential and viscous flow decomposition method for wave-structure interaction simulation with single-phase potential flow wave models and two-phase Computational Fluid Dynamics (CFD) solvers. The potential part - represents the incident waves - is solved with spectral wave models; the viscous part - represents the complementary perturbation on the incident waves - is solved with the CFD solver. This combination keeps the efficiency and accuracy of potential theory on water waves and the advantage of two-phase CFD solver on complex flows (wave breaking, flow separation, etc.). The decomposition strategy is called Spectral Wave Explicit Navier-Stokes Equations (SWENSE) [36], originally proposed for single-phase CFD solvers. Firstly, this paper presents an extension of the SWENSE method for two-phase CFD solvers. Secondly, an accurate and efficient method to interpolate potential flow results obtained by the High Order Spectral (HOS) wave model on CFD mesh is proposed. The method is able to reduce the divergence error of the interpolated velocity field to meet the CFD solver's needs without reprojection. Implemented within OpenFOAM[®], these methods are tested by three convincing verification, validation and application cases, considering incident wave propagation, high-order loads on a vertical cylinder in regular waves, and a Catenary Anchor Leg Mooring (CALM) buoy in both regular and irregular waves. Speed-ups between 1.71 and 4.28 are achieved with the test cases. The wave models and the interpolation method are released open-source to the public.

Keywords: wave-structure interaction, potential-viscous flow coupling, SWENSE, two-phase flow, spectral wave models

1 Introduction

The accurate prediction of wave-structure interactions is of vital importance in ship hydrodynamics and ocean engineering. For ocean-going vessels, the wave-induced loads are essential for analyzing ships' seakeeping property, the resistance in waves, and the structural integrity in extreme sea states. In ocean engineering, the calculation of wave-structure interaction helps to optimally design offshore structures, for example, oil and gas facilities or marine renewable energy devices.

*Corresponding author: benjamin.bouscasse@ec-nantes.fr

Traditionally, water waves and wave-structure interactions are addressed with single-phase potential theory (PT) with the perfect fluid and irrotational flow assumption. The majority of wave models - from the simplest 1st order Stokes wave theory [84] to more complex fully nonlinear theories [28, 73] - and a large number of numerical solvers for wave-structure interactions - using the Boundary Element Method (BEM) [11, 12, 66], the Finite Element Method (FEM) [57], the Finite Difference Method (FDM) [13], the Finite Volume Method (FVM) [60], the Harmonic Polynomial Cells (HPC) [81], etc - are developed based on PT. Thanks to the irrotational flow assumption, the velocity vector of flow (3 variables in 3D cases) can be represented by a scalar (the velocity potential), hence the computational complexity is much reduced. PT solvers are often considered to be more efficient than Navier-Stokes (NS) equation based solvers. However, due to the irrotational assumption, PT fails in complex scenarios, such as flow separation around structures and wave breaking.

In contrast, Computational Fluid Dynamics (CFD) solvers, based on NS equations, have a more sophisticated mathematical model and accept rotational flow. Moreover, CFD solvers offer more possibilities to deal with the water-air interface: the flow is either treated as a single-phase problem containing only water with a moving free surface boundary [15, 59, 72] or modeled as a two-phase flow containing both water and air with an interface [17, 45, 69]. The latter makes CFD solvers advantageous for violent free surface deformations, such as wave breaking, wave impact, etc. Numerous validations have proved that viscous CFD solvers are able to provide high-fidelity results for a wide variety of marine and offshore applications [83]. However, CFD solvers demand higher computational cost than PT solvers. A recent blind test [70] reveals a comparison between several CFD and PT solvers on a wave-structure interaction with an intermediate wave steepness (without wave breaking) and concludes that even the quickest CFD code is 1.5 orders of magnitude slower than a FEM-PT solver in that non-violent wave case. But the authors of [70] also admit that CFD solvers may win the comparison when the non-breaking and irrotational conditions of PT are violated, i.e., when the wave becomes larger.

To summarize, each method has advantages and limits. If they can be coupled appropriately, one can expect the resulting method to benefit from both sides. In the literature, this idea has been explored by many researchers. Among others, two main coupling strategies are commonly used: domain decomposition (DD) and functional decomposition (FD).

DD splits the computational domain into a potential region and a viscous region, and in each region, uses the appropriate solver with the best efficiency and accuracy. From a physical point of view, the complex interaction, e.g., viscous effects and violent free-surface deformation, appears near the structure only; in the far-field, the viscous effects can often be neglected, allowing the use of potential theory. For this reason, the computational domain can be split into a viscous inner sub-domain plus an irrotational outer sub-domain. Information is exchanged on the common boundary, either in a two-way interactive fashion or a one-way forcing manner. For two-way coupling: the most common practice is to couple a PT solver and a Reynolds Averaged Navier-Stokes Equation (RANSE) solver. If the structure does not induce wave breaking, both PT and RANSE solvers can be single-phase solvers as in [14, 16, 89]. When the waves near structure are more violent, two-phase RANSE solvers are more suitable, but in the far-field single-phase PT solver can still be used, as shown in [55, 82]. In extreme violent free surface deformation case (such as dam breaking), both PT and RANSE solvers are two-phase, as in [21]. The two-way coupling reduces the size of the viscous computational domain, but it requires iterations between the PT and the CFD solver, which in return needs extra efforts. The alternative one-way manner sends information from the PT to the viscous CFD solver only. The PT solver considers the wave propagation in the far-field until the inner zone. The inner CFD zone then uses this information as wave making boundary conditions. This method has been applied for shoaling and breaking wave problem in near-shore areas [40, 41, 50], calculation of wave force on offshore structures [17, 20, 68]. Several authors [42, 47] proposed a general one-way coupling method to combine potential wave theories and two-phase viscous solvers in OpenFOAM[®], which has been widely used by the

offshore and coastal engineering community. However, the one-way coupling needs a larger computational domain to avoid wave reflection [53].

The second category, FD, splits the total flow problem into (i) an irrotational part to be solved with PT solvers and (ii) a complementary part to be solved by CFD codes [24]. Since such a decomposition is not unique, multiple choices exist in the literature, which can be classified into two categories, according to the complexity of the irrotational part. One can first use PT solvers to obtain an irrotational solution of the wave-structure interaction and then correct the solution with a rotational part calculated with a CFD solver solving a complementary equation, as proposed in [32, 49, 74]. However, a more simple decomposition is to use the PT solver for the incident waves only and solve all the complementary phenomena by the CFD solver, as proposed in [36]. The FD methods usually allow the CFD solver to use coarse mesh in the far-field to reduce the computational cost, since the interesting zone of the complementary phenomena locates often near the structure only.

The Spectral Wave Explicit Navier-Stokes Equations (SWENSE) method presented in this paper belongs to the FD category and it decomposes the total solution into an incident wave part and a complementary part. The essential benefits of the method are: (i) the fast and accurate incident wave simulation and (ii) that it allows the use of coarse mesh in the far-field region while keeping the near-field accuracy. A refined mesh is required only near the structure where the complementary field needs to be solved accurately. The original SWENSE method is proposed only for single-phase CFD solvers. It has been successfully applied to calculate wave force on vertical cylinder [52], on a Catenary Anchor Leg Mooring Buoy [62], and ship resistance in waves [72]. In the single phase scenario, the use of coarser mesh reduced the CPU time of the SWENSE method by one order of magnitude compared with conventional NS solvers for an equivalent accuracy [56].

Recently, the SWENSE method has been extended for two-phase CFD solvers [87]. However, reference [87] adopts a FD strategy different from the original SWENSE method, which leaves the pressure field undecomposed. Consequently, the use of coarse mesh in the far-field may introduce errors to the incident pressure field and also to the incident waves, losing the advantage of the SWENSE method. This point will be discussed in detail in Sect. 2.4.3.

In this paper, we present a novel extension of the SWENSE method for two-phase viscous CFD solvers, which keeps all advantages of the original method, i.e. the ability to use a coarse mesh in the far-field to enhance the efficiency. Moreover, coupling two-phase CFD solvers with SWENSE enables the method to deal with violent free surface deformations, such as breaking waves near the structure. Secondly, the paper also proposes an accurate and convenient reconstruction method to interpolate the results of High-Order Spectral (HOS) wave models onto CFD mesh. The method can reduce the divergence error of the interpolated velocity field to meet the CFD solver's need without reprojection. Implemented in OpenFOAM[®], the validity and efficiency of the proposed methods are assessed thanks to three convincing cases, including the simulation of progressive regular waves, the calculation of high order loads on a vertical cylinder in regular waves, and a Catenary Anchored Leg Mooring (CALM) buoy in regular and irregular waves.

The rest of the paper is organized as follows. Section 2 derives the two-phase SWENS governing equations and compares them with those of reference [87]. Section 3 presents the fully non-linear spectral wave models for incident wave modeling and proposes the reconstruction technique to interpolate the results of HOS wave models to CFD mesh. Section 4 details the numerical discretization and an implementation example of a two-phase SWENSE solver in OpenFOAM[®] [7]. The validation and application cases are shown in Sect. 5.

2 Governing equations of the two-phase SWENSE method

2.1 SWENSE decomposition

The SWENSE method [36, 37] defines three notions in a wave-structure interaction:

1. Total field: the total field represents the real flow including the incident waves, the scattered waves and viscous effects caused by the wave-structure interaction. It is assumed that the flow is governed by the incompressible (NS) equations.
2. Incident field: the incident part concerns the propagation of the incident waves in the computational domain without structures. The viscosity is neglected. The flow is described by the Euler equations. It is further assumed that the flow is irrotational so that incident waves can be solved by PT wave models.
3. Complementary field: the complementary part represents the difference between the total field and the incident field. This field is generated due to the presence of structures in the computational domain and the viscosity of the fluid. The complementary variables are governed by the SWENS equations.

With these notions, a primitive field of the flow χ (pressure, velocity) is decomposed into an incident part χ_I and a complementary part χ_C (see Eqn. 1). χ_I is explicitly given by PT wave models; χ_C is to be calculated by the CFD solver implementing the SWENS equations. In the following contents, variables without subscript denote the total field, subscript I denotes the incident part, and subscript C denotes the complementary part.

$$\chi = \chi_I + \chi_C \quad (1)$$

In Fig. 1, a V-shape illustrates how the SWENS equations are derived with the functional decomposition and how the total field is reconstructed. The left half of this V-shape shows the derivation procedure of the SWENS equations. Assuming the Navier-Stokes equations (the first row) and the Euler equations (the second row) have the same definition zone, we can subtract the Euler equations from the NS equations. The SWENS equations (the third row) is obtained by writing the remainder with the variable χ_C . On the right half, the complementary field χ_C is added to the incident solution χ_I to reconstruct the total solution χ .

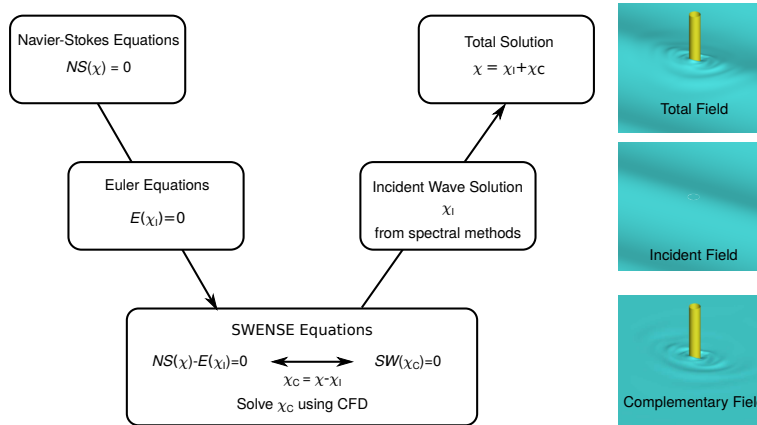


Figure 1: The functional decomposition in the SWENSE method

2.2 Derivation of two-phase SWENS equations

The two-phase SWENS equations are derived following the SWENSE decomposition procedure in Fig. 1 with the two-phase NS equations and the Euler equations.

2.2.1 Two-phase incompressible Navier-Stokes equations

In the present work, the immiscible air-water flow with a deformable common interface is considered as incompressible and viscous. The definition zone contains both water and air.

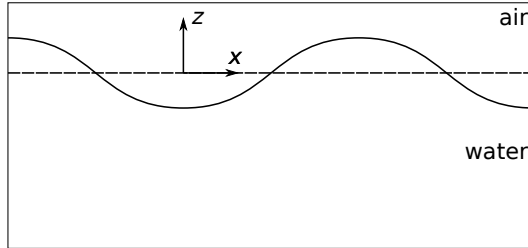


Figure 2: The definition zone of the two-phase NS equations: both water and air are considered.

The Volume-of-Fluid (VOF) method [43] is used for interface capturing. The method is chosen among others for its advantage of mass conservation. The VOF field α is used to represent the volume fraction of water. It is transported by the total velocity field \mathbf{u} with the following equation:

$$\frac{\partial \alpha}{\partial t} + \nabla \cdot (\mathbf{u}\alpha) + \nabla \cdot (\mathbf{u}_r \alpha (1 - \alpha)) = 0 \quad (2)$$

where $\mathbf{u} = (u, v, w)$ is the fluid velocity, and $\nabla \cdot (\alpha(1 - \alpha)\mathbf{u}_r)$ is an artificial compression term to avoid the interface smearing with \mathbf{u}_r the compression velocity [10, 76]. A sharp interface is approximated with $\alpha = 0.5$. The density ρ and the molecular viscosity μ are phase-dependent and are defined as:

$$\rho = \begin{cases} \rho_w & \alpha > 0.5 \\ \rho_a & \alpha \leq 0.5 \end{cases} \quad (3)$$

and

$$\mu = \begin{cases} \mu_w & \alpha > 0.5 \\ \mu_a & \alpha \leq 0.5 \end{cases} \quad (4)$$

with subscriptions w and a representing water and air respectively. This kind of definition has been used in the literature [9, 48]. Despite its simplicity, it shows adequate accuracy in the present work, while other more accurate techniques (such as PLIC [77]) can be considered in the future.

The flow is described by incompressible NS equations.

$$\nabla \cdot \mathbf{u} = 0 \quad (5)$$

$$\frac{\partial \mathbf{u}}{\partial t} + \mathbf{u} \cdot \nabla \mathbf{u} = -\frac{\nabla p}{\rho} + \mathbf{g} + \frac{\nabla \cdot ((\mu + \mu_t)(\nabla \mathbf{u} + \nabla \mathbf{u}^T))}{\rho} \quad (6)$$

where p is the total pressure; \mathbf{g} is the gravitational acceleration; μ_t represents the turbulent viscosity, obtained from Reynolds averaged turbulence models with the Boussinesq assumption. Eqn. (6) neglects the surface tension since it is small in classical marine and ocean engineering applications.

2.2.2 Euler equations for incident water waves

The incident waves are modeled as a single-phase flow. The water free surface is considered as a moving boundary (see Fig. 3). and is defined by a time-dependent free-surface elevation function, as follows

$$z = \eta_I(\tilde{\mathbf{x}}, t) \quad (7)$$

where $\tilde{\mathbf{x}} = (x, y)$. It assumes η_I is a single-valued function, and the application is consequently limited to non-breaking incident waves.

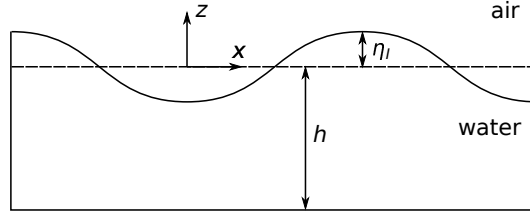


Figure 3: The definition zone of the single-phase Euler equations: only water is considered. Water waves are modeled as a single-phase problem with a deforming free surface.

Neglecting the viscosity of water, the flow beneath the free surface is modeled with the incompressible Euler equations, as follows,

$$\nabla \cdot \mathbf{u}_I = 0 \quad (8)$$

$$\frac{\partial \mathbf{u}_I}{\partial t} + \mathbf{u}_I \cdot \nabla \mathbf{u}_I = -\frac{\nabla p_I}{\rho_I} + \mathbf{g} \quad (9)$$

where the subscript I represents “*incident*” field. The density ρ_I is equal to the water density since the equations are defined only in water. The boundary conditions are:

$$\frac{\partial \eta_I}{\partial t} + u_I \frac{\partial \eta_I}{\partial x} + v_I \frac{\partial \eta_I}{\partial y} - w_I = 0 \quad \text{at } z = \eta_I(\tilde{\mathbf{x}}, t) \quad \text{on the free surface} \quad (10)$$

$$p_I = 0 \quad \text{at } z = \eta_I(\tilde{\mathbf{x}}, t) \quad \text{on the free surface} \quad (11)$$

$$w_I = 0 \quad \text{at } z = -h \quad \text{on the seabed} \quad (12)$$

with $\mathbf{u}_I = (u_I, v_I, w_I)$ and $\tilde{\mathbf{x}} = (x, y)$.

Extension of the definition zone

It is worth noting that the definition zone of Euler equations is different from that of two-phase NS equations. Consequently, the former must be extended to apply the same SWENSE decomposition in both water and air. The extension technique will be presented in Sect. 3.3. Herein, please just assume the Euler equations and their solution have the same definition zone as that of the two-phase NS equations, i.e., in the whole air-and-water domain.

2.2.3 Two-phase Spectral Wave Explicit Navier-Stokes Equations

The two-phase SWENS equations are derived by subtracting the Euler equations from the two-phase Navier-Stokes equations.

Continuity Equation

Using the continuity equation of NS equations (Eqn. 5) minus the that of Euler equations (Eqn. 8), yields:

$$\nabla \cdot (\mathbf{u} - \mathbf{u}_I) = 0 \quad (13)$$

With the notation of $\mathbf{u}_C = \mathbf{u} - \mathbf{u}_I$, the continuity equation using the complementary variable reads:

$$\nabla \cdot \mathbf{u}_C = 0 \quad (14)$$

Momentum Equation

The momentum equation should also be derived by subtracting the momentum equation of the Euler equations (Eqn. 9) from that of the Navier-Stokes equations (Eqn. 6). However, the direct use of Eqn. (9) causes stability problems in the air (see Appendix A). For this reason, Eqn. (9) is modified by introducing a pressure term p_I^* :

$$p_I^* = \rho \frac{p_I}{\rho_I} \quad (15)$$

where ρ is the density of the two-phase flow and ρ_I is equal to the water density. Eqn. (9) written in its modified version by using p_I^* reads:

$$\frac{\partial \mathbf{u}_I}{\partial t} + \mathbf{u}_I \cdot \nabla \mathbf{u}_I = -\frac{\nabla p_I^*}{\rho} + \frac{p_I}{\rho_I} \frac{\nabla \rho}{\rho} + \mathbf{g} \quad (16)$$

Subtracting Eqn. (16) from Eqn. (6) and using the notation of $p_C = p - p_I^*$ the two-phase SWENSE momentum equation written with the complementary variables is obtained as:

$$\frac{\partial \mathbf{u}_C}{\partial t} + \mathbf{u} \cdot \nabla \mathbf{u}_C + \mathbf{u}_C \cdot \nabla \mathbf{u}_I = -\frac{\nabla p_C}{\rho} - \frac{p_I}{\rho_I} \frac{\nabla \rho}{\rho} + \frac{\nabla \cdot ((\mu + \mu_t) (\nabla \mathbf{u} + \nabla \mathbf{u}^T))}{\rho} \quad (17)$$

We now simplify the viscosity term, by separating the molecular and turbulent terms. Looking at the molecular terms first, we can decompose it into incident and complementary terms.

$$\nabla \cdot (\mu (\nabla \mathbf{u} + \nabla \mathbf{u}^T)) = \nabla \cdot (\mu (\nabla \mathbf{u}_I + \nabla \mathbf{u}_I^T)) + \nabla \cdot (\mu (\nabla \mathbf{u}_C + \nabla \mathbf{u}_C^T)) \quad (18)$$

Continue to simplify the incident part using $\nabla \cdot \mathbf{u}_I = 0$ and $\nabla \times \mathbf{u}_I = 0$, since the incident velocity field is incompressible and irrotational. we have

$$\begin{aligned} \nabla \cdot (\mu (\nabla \mathbf{u}_I + \nabla \mathbf{u}_I^T)) &= 2 \nabla \cdot (\mu \nabla \mathbf{u}_I^T) \\ &= 2 (\mu \nabla (\nabla \cdot \mathbf{u}_I) + \nabla \mathbf{u}_I \cdot \nabla \mu) \\ &= 2 \nabla \mathbf{u}_I \cdot \nabla \mu. \end{aligned} \quad (19)$$

The turbulence viscosity can be also simplified in the same way, the resulting equation is:

$$\frac{\partial \mathbf{u}_C}{\partial t} + \mathbf{u} \cdot \nabla \mathbf{u}_C + \mathbf{u}_C \cdot \nabla \mathbf{u}_I = -\frac{\nabla p_C}{\rho} - \frac{p_I}{\rho_I} \frac{\nabla \rho}{\rho} + \frac{\nabla \cdot ((\mu + \mu_t) (\nabla \mathbf{u}_C + \nabla \mathbf{u}_C^T))}{\rho} + \frac{2 \nabla \mathbf{u}_I \cdot \nabla \mu}{\rho} + \frac{2 \nabla \mathbf{u}_I \cdot \nabla \mu_t}{\rho} \quad (20)$$

It worth noting that in Eqn. (20), two source terms have non-zero values only on the air-water interface, i.e., $\frac{p_I}{\rho_I} \frac{\nabla \rho}{\rho}$ and $\frac{2 \nabla \mathbf{u}_I \cdot \nabla \mu}{\rho}$. The first suggests a restoring force proportional to the density gradient. The

second represents a viscous dissipation at the interface, which is proportional to the molecular viscosity gradient. The second term is neglected since it is several orders of magnitude smaller. Moreover, the turbulence stress on the incident wave part is also neglected $\left(\frac{2\nabla\mathbf{u}_I \cdot \nabla\mu_t}{\rho}\right)$, because we assume the incident waves provided by PT solver is accurate for the aspect of application and should not interact with the turbulence viscosity.

The final simplified momentum equation reads,

$$\frac{\partial\mathbf{u}_C}{\partial t} + \mathbf{u} \cdot \nabla\mathbf{u}_C + \mathbf{u}_C \cdot \nabla\mathbf{u}_I = -\frac{\nabla p_C}{\rho} - \frac{p_I}{\rho_I} \frac{\nabla\rho}{\rho} + \frac{\nabla \cdot ((\mu + \mu_t)(\nabla\mathbf{u}_C + \nabla\mathbf{u}_C^T))}{\rho} \quad (21)$$

VOF Equation

The VOF field is not decomposed as other variables because it is challenging to consider the boundedness in the decomposition, i.e., it is not straightforward to define an incident VOF field α_I and a complementary VOF field α_C and to keep $0 \leq \alpha_I + \alpha_C \leq 1$. Instead, the total VOF field is transported with the reconstructed total field $\mathbf{u} = \mathbf{u}_I + \mathbf{u}_C$ using Eqn. (2). The authors are aware that in this step (transporting VOF field with a given velocity field), the proposed method introduces numerical errors as large as convectional two-phase VOF NS solvers, and thus may restrict the accuracy of the present method when using coarse mesh. However, the mesh requirement of an accurate VOF convection is often not as demanding as for the momentum equations (see Appendix B): using 15 cells per wave length can already provide adequate accuracy. Decomposition approaches can be used on other approaches such as the Decomposed Level-Set (DLS) [71, 87]. Appendix B also provides a comparison between VOF and DLS.

2.3 Boundary conditions

The boundary conditions (BCs) of the complementary field are derived from the boundary conditions of the total fields, with the same physical significance. Table 1 shows some commonly used BCs in the SWENSE method with their equivalence in Navier-Stokes Equation (NSE).

For far-field and the non-slip wall boundary condition, the BCs of NSE and SWENSE are mathematical equivalent. The pressure BCs are not given, as they should be calculated to ensure the fixed velocity BC. The far-field BC is applied to the outer boundaries, assuming that the fluid motion is equal to the incident waves, i.e., the complementary field vanishes because the wave amplitude decay with $1/\sqrt{r}$ (r is the distance from the structure). The no-slip wall BC is used on the body. For a fixed body, the total velocity on the wall $\mathbf{u} = 0$, thus in SWENSE $\mathbf{u}_C = -\mathbf{u}_I$.

The atmosphere boundary is the upper limit of the computational domain in two-phase flow simulation, which is connected to the atmosphere. In NSE, such boundary condition is imposed by the atmosphere pressure ($p = 0$) and assumes the gradient of velocity \mathbf{u} is equal to zero. The strict equivalence is $p_C = -p_I^*$. However, the p_I^* is small by definition in the air (Eqn. (15)). For simplicity, we impose $p_C = 0$ and assume the gradient of \mathbf{u}_C is zero.

Table 1: Boundary conditions of SWENSE compared with Navier-Stokes Equations

	NSE	SWENSE
Far-field	$\alpha = \alpha_I$	$\alpha = \alpha_I$
	$\mathbf{u} = \mathbf{u}_I$	$\mathbf{u}_C = \mathbf{0}$
No-slip wall	$\frac{\partial \alpha}{\partial n} = 0$	$\frac{\partial \alpha}{\partial n} = 0$
	$\mathbf{u} = \mathbf{0}$	$\mathbf{u}_C = -\mathbf{u}_I$
Atmosphere	$\frac{\partial \alpha}{\partial n} = 0$	$\frac{\partial \alpha}{\partial n} = 0$
	$p = 0$	$p_C = 0$
	$\frac{\partial \mathbf{u}}{\partial n} = \mathbf{0}$	$\frac{\partial \mathbf{u}_C}{\partial n} = \mathbf{0}$

2.4 Discussion

2.4.1 Relation with NS equations

The given SWENSE equation can regress to the NS equations when the incident solution is set to be calm water, i.e., Eqn. (21) in the two-phase SWENSE momentum equation is equivalent to Eqn. (6) in the two-phase NS Equations, if the incident wave part is explicitly given as no waves.

To prove that, one can let the incident wave field be zero, i.e.:

$$\mathbf{u}_I = 0 \quad (22)$$

and thus the incident pressure is equal to the hydrostatic pressure:

$$\frac{p_I}{\rho_I} = -gz \quad (23)$$

Thus, Eqn. (21) can be written as:

$$\frac{\partial \mathbf{u}_C}{\partial t} + \mathbf{u} \cdot \nabla \mathbf{u}_C = -\frac{\nabla p_C}{\rho} + gz \frac{\nabla \rho}{\rho} + \frac{\nabla \cdot ((\mu + \mu_t) (\nabla \mathbf{u}_C + \nabla \mathbf{u}_C^T))}{\rho} \quad (24)$$

Transforming this equation with the relations below:

$$\mathbf{u}_C = \mathbf{u} - \mathbf{u}_I = \mathbf{u} \quad (25)$$

$$p_C = p - p_I^* = p + \rho gz \quad (26)$$

yields Eqn. 6, showing that the SWENSE momentum equation (Eqn. 21) can regress to the two-phase NS equation (Eqn. 6) if there are no incident waves.

2.4.2 Keeping incident solution with coarse mesh

The second property is to preserve exactly the incident wave solution throughout the domain when no structure is present, regardless of the mesh used.

In the case of pure incident wave simulation, the initial values of the complementary fields are zero, i.e.:

$$\mathbf{u}_C(\mathbf{x}, t = 0) = 0 \quad (27)$$

$$p_C(\mathbf{x}, t = 0) = 0 \quad (28)$$

The second term on the R.H.S of Eqn. (21) is equal to zero in the entire computational domain,

$$\frac{p_I}{\rho_I} \frac{\nabla \rho}{\rho} = 0 \quad (29)$$

because

	At the incident free-surface	elsewhere
p_I	0	non-zero
$\nabla \rho$	non-zero	0
$\frac{p_I}{\rho_I} \frac{\nabla \rho}{\rho}$	0	0

Using the above conditions, Eqn. (21) is simplified to:

$$\frac{\partial \mathbf{u}_C}{\partial t} = 0 \quad (30)$$

showing that complementary velocity fields \mathbf{u}_C remains zero. In this condition, the pressured field p_C also remains zero after solving the pressure Poisson equation. As a result, Eqn. (21) preserves the kinematics of the incident waves.

2.4.3 Main differences from Vukčević *et al.* [87]

Another two-phase SWENSE method has been introduced early by Vukčević *et al.* [87] with different characteristics with the method proposed here. These differences are presented as follows.

The first and the fundamental difference is that in reference [87], terms containing incident wave information are not simplified with known relations from PT. For example, the continuity equation used in reference [87] reads,

$$\nabla \cdot \mathbf{u}_C = -\nabla \cdot \mathbf{u}_I. \quad (31)$$

Although the R.H.S. is equal to zero in the wave theory, reference [87] evaluates it by the CFD solver, to consider the errors coming from:

- the spectral solution techniques;
- the interpolation of incident wave velocity on the CFD mesh.

Reference [87] emphasizes the necessity to correct these errors with the complementary field. However, in the present work, we choose to drop off these errors and cancel out the R.H.S. term with the theoretical relation $\nabla \cdot \mathbf{u}_I = 0$ for incompressible flow. The reasons for this choice are:

- The PT methods are accurate for water wave problems. The numerical error resides in a converged spectral potential flow result is often negligible. Compensating this error by CFD solvers is not beneficial because this correcting step may introduce larger numerical errors itself.

- The interpolation of incident field on CFD mesh is improved in this work (see Section 3.2), so that the numerical error related to the interpolation procedure is drastically reduced.
- The numerical evaluation of the incident quantities requires fine CFD discretization to be accurate. This is not consistent with the objective of the SWENSE method, i.e., to use coarse mesh for the incident wave propagation problem.

Similarly, the momentum equation (Eqn. 32) in reference [87] is not simplified either with the analytic relation provided by the Euler equations. It reads,

$$\frac{\partial \mathbf{u}_C}{\partial t} + \mathbf{u} \cdot \nabla \mathbf{u}_C - \nu \nabla^2 \mathbf{u}_C = -\frac{\partial \mathbf{u}_I}{\partial t} - \mathbf{u} \cdot \nabla \mathbf{u}_I + \nu \nabla^2 \mathbf{u}_I - \beta \nabla p_d \quad (32)$$

where ν is the kinematic viscosity and $\beta = 1/\rho$. This treatment also prevents the use of coarse mesh for incident wave propagation, because coarse mesh (even only used in the far-field) generates errors on the R.H.S. of Eqn. (32) and results in spurious complementary fields that interfere with incident waves. In contrast, the present work cancels out these terms with analytical relations so that the numerical errors can be avoided, as shown in Sect. 2.4.2.

The second difference is that reference [87] uses the Decomposed Level Set (DLS) method to capture the interface, instead of the standard VOF (not decomposed) here. Appendix B compares both methods on a pure convection case, i.e., the interface capturing function is transported by the incident wave velocity. The results demonstrate that the DLS is not more advantageous than the VOF in the present second-order accurate Finite Volume framework.

3 Incident wave modeling

This section describes how to obtain the incident wave solution by potential flow solvers (spectral wave models) and how to interpolate it onto the CFD mesh.

3.1 Potential flow theory and spectral solution techniques

By further assuming the incident wave velocity is irrotational, the Euler equations can be solved efficiently and accurately [22] with PT. Such an assumption allows to reduce the number of unknowns in the Euler equation, by defining a scalar field ϕ (called velocity potential or potential), so that:

$$\mathbf{u}_I = \nabla \phi \quad (33)$$

Using ϕ , the Euler equations are written in an equivalent form, as follows,

$$\Delta \phi = 0 \quad \text{Laplace's equation} \quad (34)$$

$$\frac{\partial \eta_I}{\partial t} + \frac{\partial \phi}{\partial x} \frac{\partial \eta_I}{\partial x} + \frac{\partial \phi}{\partial y} \frac{\partial \eta_I}{\partial y} - \frac{\partial \phi}{\partial z} = 0 \quad \text{at } z = \eta_I(\mathbf{x}, t) \quad \text{Free surface kinematic condition} \quad (35)$$

$$\frac{\partial \phi}{\partial t} + \frac{1}{2}(\nabla \phi)^2 + gz = 0 \quad \text{at } z = \eta_I(\mathbf{x}, t) \quad \text{Free surface dynamic condition} \quad (36)$$

$$\frac{\partial \phi}{\partial z} = 0 \quad \text{at } z = -h \quad \text{Seabed boundary condition} \quad (37)$$

In the present work, spectral methods are used to solve this non-linear potential flow problem with high accuracy and efficiency. These methods decompose the free surface elevation $\eta_I(\tilde{\mathbf{x}}, t)$ and the velocity

potential $\phi(\tilde{\mathbf{x}}, z, t)$ using a set of basis functions. An example in a 2D uni-directional wave case is shown as follows:

$$\eta_I(x, t) = \sum_i A_i^\eta(t) \psi_i(x) \quad (38)$$

$$\phi(x, z, t) = \sum_i A_i^\phi(t) \frac{\cosh(k_i(z+h))}{\cosh(k_i h)} \psi_i(x) \quad (39)$$

where A_i are the modal amplitudes, k_i are the basis wave numbers, and $\psi_i(x)$ are the horizontal basis functions (sine and cosine functions or their complex exponential equivalents). With these basis functions, Eqn. (39) satisfy automatically the Laplace's equations and the seabed boundary condition (Eqns. 34 and 37). The free surface boundary conditions (Eqns. 35 and 36), discretized on uniformly distributed points on the free surface, are used to establish a linear system to determine the modal amplitudes $A_i^\eta(t)$ and $A_i^\phi(t)$.

In this work, two fully non-linear spectral methods are adopted. The first is based on the stream function waves theory [30, 73] for 2D regular waves. The second is the High-Order Spectral (HOS) method [27, 28] for 2D/3D arbitrary waves in open seas or in experimental wave tanks.

3.1.1 Regular waves: stream function theory

For 2D regular nonlinear waves, the algorithm proposed by Rienecker & Fenton [73] based on the stream function theory is adopted [4, 30]. This algorithm solves 2D progressing regular waves over a horizontal seabed for a wide range of depths, amplitudes and wavelengths. The free surface elevation and the velocity potential are decomposed with basis functions as shown in Eqns. (38) and (39). The basis function $\psi_i(x)$ is replaced by $\psi_i(x - ct)$, with c the phase velocity to make the modal amplitudes A_i^η and A_i^ϕ independent of time. These amplitudes are solved from a linear system established with the kinematic and the dynamic boundary conditions (Eqns. 35 and 36). The velocity field \mathbf{u}_I is calculated with Eqn. (33), and the pressure field is obtained with the Bernoulli equation. The reader can find more information in references [73].

3.1.2 Arbitrary waves: High-Order Spectral method

The High-Order Spectral (HOS) method is widely used for the study of arbitrary waves wave propagating in open domains [25, 88]. It considers the full non-linearity of the free surface and exhibits high efficiency and accuracy thanks to its pseudo-spectral formalism. Two open-source solvers developed at LHEEA Lab. (Ecole Centrale Nantes and CNRS), *HOS-Ocean* [3, 28] and *HOS-NWT* [2, 27], are used to solve arbitrary incident waves in open domains and experimental wave tanks, respectively.

For simplicity, only *HOS-Ocean* in a 2D case is presented as an example. The reader is referred to references [27, 28] for more information.

The HOS wave model solves an unsteady wave propagation problem with the following equations derived from the free surface boundary conditions (Eqns. 35 and 36) to describe the time evolution of the free surface elevation η_I and the velocity potential $\tilde{\phi}$.

$$\frac{\partial \eta_I}{\partial t} = \left(1 + \left(\frac{\partial \eta_I}{\partial x} \right)^2 \right) w_I - \frac{\partial \tilde{\phi}}{\partial x} \cdot \frac{\partial \eta_I}{\partial x} \quad (40)$$

$$\frac{\partial \tilde{\phi}}{\partial t} = -g\eta_I - \frac{1}{2} \left(\frac{\partial \tilde{\phi}}{\partial x} \right)^2 + \frac{1}{2} \left(1 + \left(\frac{\partial \eta_I}{\partial x} \right)^2 \right) w_I^2 \quad (41)$$

where x is the horizontal coordinate, $\tilde{\phi}$ is the free surface velocity potential defined as follows:

$$\tilde{\phi}(x, t) = \phi(x, z = \eta_I(x, t), t) \quad (42)$$

$\tilde{\phi}$ is decomposed in the spectral domain with the following equation:

$$\tilde{\phi}(x, t) = \sum_{i=1}^N A_i^{\tilde{\phi}}(t) \exp(jk_i x) \quad (43)$$

where j is the unit imaginary number $j^2 = -1$. The free surface elevation η_I is decomposed with Eqn. (38). Such a decomposition allows the efficient calculation of η_I and $\tilde{\phi}$ and their spatial derivatives on a series of uniformly distributed HOS calculation points with the Fast Fourier Transform (FFT).

Figure 4 gives an example of an irregular sea state simulation conducted with *HOS-Ocean* [3]. The computational domain and time duration are made to be large enough for investigating the occurrence of extreme wave events. The irregular sea state is generated using a Joint North Sea Wave Project (JONSWAP) spectrum. The size of the domain is $(Lx, Ly) = (40\lambda_p, 20\lambda_p) \approx 50 \text{ km}^2$.

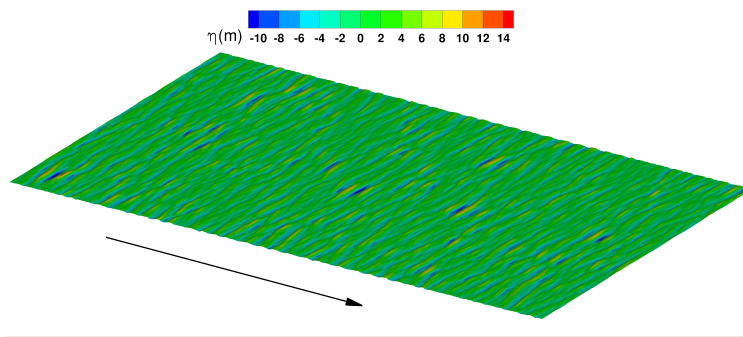


Figure 4: Free-surface elevation of a *HOS-Ocean* simulation with a JONSWAP spectrum. The size of computational domain is about 50 km^2 . The picture is reproduced from the work of Ducrozet *et al.* [28]. Reprinted with permission, copyright Elsevier®.

Besides *HOS-Ocean*, the second solver, *HOS-NWT* (Numerical Wave Tank) [2, 27], is used to reproduce wave evolution in experimental test basins. The basis functions and the numerical schemes are adapted to reproduce a rectangular wave tank with a 3D wave-maker, an absorbing beach, and perfectly reflective side walls.

3.2 Reconstruction of incident wave information on the CFD mesh

The reconstruction step transforms the results of spectral wave models onto the CFD mesh. For example, in a 2D case, the velocity potential ϕ is stored as the modal amplitudes $A_i^{\phi}(t)$ in Eqn. (39). With these modal amplitudes, the potential ϕ can be reconstructed and the velocity can be further calculated by evaluating the derivatives of the potential (Eqn. 33) as follows:

$$u_I(x, z, t) = \sum_{i=1}^N A_i^{\phi}(t) j k_i \frac{\cosh(k_i(z+h))}{\cosh(k_i h)} \psi_i(x) \quad (44)$$

$$w_I(x, z, t) = \sum_{i=1}^N A_i^{\phi}(t) k_i \frac{\sinh(k_i(z+h))}{\cosh(k_i h)} \psi_i(x) \quad (45)$$

The velocity can be obtained by substituting the coordinates (x, z) and the time t into the above equations. This reconstruction method is referred to as “analytical evaluation” method hereafter. The computational cost at each cell location and at each timestep is proportional to the number of Fourier components. For the stream function wave theory, the number of Fourier components are $N \approx O(10)$, whereas the HOS method typically needs 100 to 1000 Fourier components in a single direction for an irregular wave train. As a result, the analytical evaluation is very time-consuming for HOS waves. Instead, an interpolation method is used: the modal results are first transferred on a series of space points with the Inverse Fast Fourier Transform (IFFT) algorithm and then interpolated to the CFD cells. In this section, the analytical evaluation and the interpolation method are explained in the first two subsections. The third subsection focuses on the reconstruction error and its consequences. The last subsection proposes a new interpolation technique to improve the interpolation accuracy. For simplicity, only the velocity field is shown as an example. The pressure field can be reconstructed similarly.

3.2.1 Analytical evaluation for the stream function wave theory

For regular waves obtained with the stream function wave theory, the analytical evaluation method is applied since the number of Fourier components is small. For example, a regular wave with a moderately large steepness ($ka = 0.24$) converges with only 9 Fourier components ($N = 9$).

3.2.2 Interpolation for the HOS waves

The interpolation procedure [26] to reconstruct the HOS results on CFD cells firstly reconstructs the wave information on a coarse rectangular HOS grid via IFFT and then interpolates it on the CFD mesh. Compared to the analytical evaluation, the efficiency is much improved by the IFFT algorithm. This procedure can be divided into two steps.

1. IFFT: This step translates the spectral information in the spatial domain via IFFT. After the IFFT, the wave information is available on uniformly spaced points. The number of points is equal to the number of Fourier modes (N) used in the HOS computation. The distance between two points is equal to the shortest wave length of the basis function ($2\pi/k_N$). Take a 2D case as an example:
 - For the free surface elevation ($\eta_I(x, t)$), IFFT transforms A_i^η to N uniformly distributed points in the x direction (see Figure 5).
 - The velocity field ($\mathbf{u}_I(x, z, t)$) is reconstructed similarly. But since the velocity field also depends on the vertical direction (z), several IFFTs are used. Each IFFT transforms A_i^ϕ to the velocity at N horizontally uniformly distributed points with a given vertical position z . After this reconstruction, the velocity field is available on a coarse rectangular grid (referred to as the “HOS grid” hereafter) with several horizontal layers. Each horizontal layer contains N uniformly distributed points. Note the vertical position of these layers can be given arbitrarily, so that a vertical refinement is possible. In contrast, horizontal refinement cannot be done directly since the number of points N is equal to the number of modes in the HOS calculation.
2. Interpolation: the incident wave information is interpolated from the HOS grid onto the CFD mesh, as the HOS grid is usually different from a CFD mesh. For example, a typical HOS simulation uses 10 points per peak wave length, while CFD solvers usually use around 100 cells. Figure 6 interpolated a comparison of a typical HOS grid (on the left) and a CFD mesh (on the right). The figure is colored by the velocity magnitude. The result on the CFD mesh is interpolated from the HOS grid behind it with the cubic spline scheme.

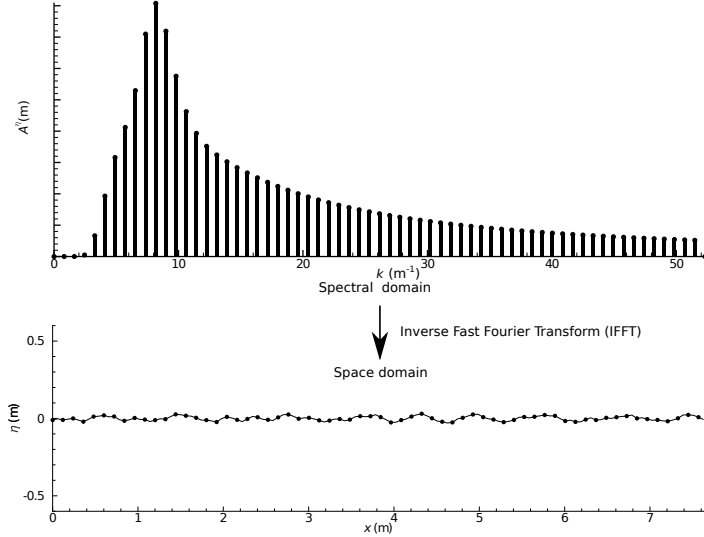


Figure 5: Reconstruction of the incident wave solution on the HOS grid. Top plot: free surface elevation (η_I) is stored in spectral domain as amplitudes of its Fourier components. Bottom plot: the modal information is transformed in the spatial domain with the Inverse Fast Fourier Transform (IFFT) on uniformly-spaced points.

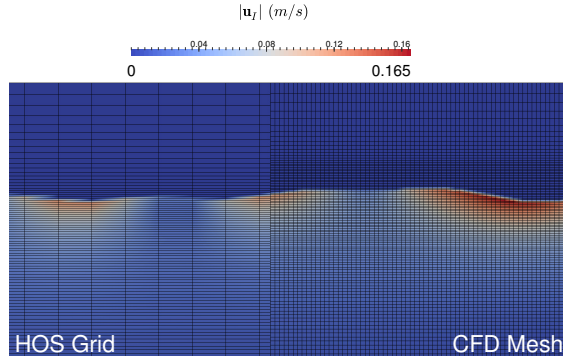


Figure 6: Comparison of a typical HOS grid having the same horizontal resolution used in the HOS simulation (left) and the mesh of a CFD solver (right).

An example of the interpolation result is shown in Fig. 7. The VOF field (on the top) is reconstructed from the free surface elevation (η_I). The velocity field is shown at the bottom. The waves are simulated by *HOS-Ocean* (JONSWAP wave spectrum with $T_p = 0.7s$, $H_s = 0.028m$, $\gamma = 3.3$). The HOS simulation domain contains 10 peak wave lengths ($L_x = 10\lambda_p$) with 128 Fourier components ($N = 128$).

3.2.3 Reconstruction error: velocity divergence

This section analyzes the reconstruction error, represented by the velocity divergence ($\nabla \cdot \mathbf{u}_I$). The physical significance of the velocity divergence is the volume change rate. Its unit is s^{-1} . Having $\nabla \cdot \mathbf{u}_I = a(s^{-1})$ means that the fluid will have a relative volume change of a in one second. If the reconstruction is accurate, the velocity divergence is equal to zero because the flow is incompressible.

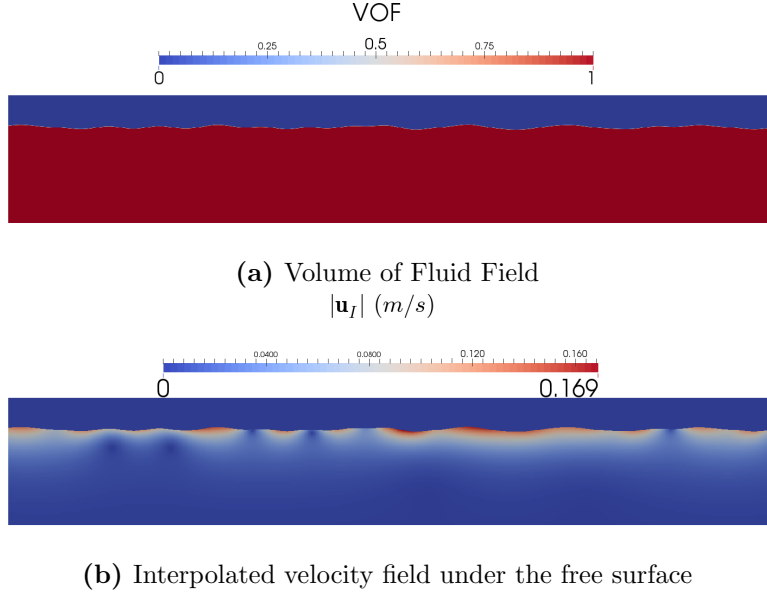


Figure 7: Irregular wave field interpolated from the HOS grid onto the CFD mesh.

The VOF method is very sensitive to the velocity divergence because the boundedness of the VOF field requires a divergence free velocity field. Such an error finally leads to instabilities in the simulation.

In the present work, the velocity field is reconstructed on Finite Volume mesh. The divergence is then calculated by:

$$\nabla \cdot \mathbf{u}_I = \sum_f \mathbf{u}_{I,f} \cdot \mathbf{A}_f / \Delta V \quad (46)$$

where f represents the cell faces, $\mathbf{u}_{I,f}$ represents the face-averaged incident velocity, \mathbf{A}_f the surface vector of the cell face f , and ΔV the volume of the cell. It may contain numerical errors coming from:

1. Approximating the face-averaged value by the face-center value ($\mathbf{u}_{I,f} \approx \mathbf{u}_I(\mathbf{x}_{cf})$), where \mathbf{x}_{cf} is the face center coordinates.
2. Evaluating $\mathbf{u}_I(\mathbf{x}_{cf})$ by interpolation in the interpolation method.

The first source of error is due to the use of the second-order Finite Volume Method, which affects both the analytical evaluation and the interpolation method and is often negligible. In contrast, the second source of error is usually much larger. Figure 8 shows the divergence error of the interpolated velocity field of Fig. 7. The CFD mesh is discretized with $(\Delta x, \Delta z) = (\lambda_p/100, H_s/20)$. The VOF field transported by this velocity field after one wave period is shown in Fig. 9. Its values are no more bounded by 0 and 1. This problem suggests the necessity to improve the interpolation accuracy.

3.2.4 Improvement of the interpolation accuracy

The main source of inaccuracy in the interpolation is the large space interval between HOS points. Refining the HOS grid is definitively helpful to reduce the interpolation error. However, using a grid as refined as a CFD mesh directly in the HOS computation is not feasible, since it introduces too many very short waves and may make the computation unstable [29]. To overcome this difficulty, we propose a refinement at the

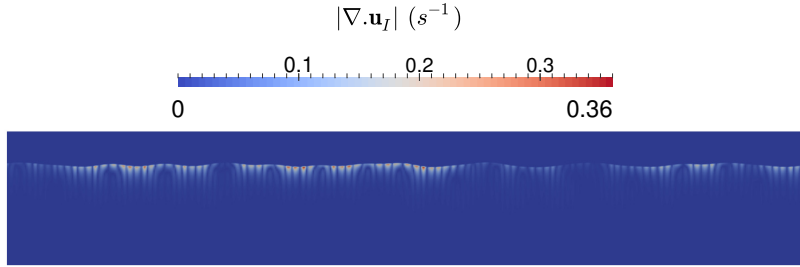


Figure 8: Divergence error of an interpolated HOS velocity field on a CFD mesh: HOS grid with 128 points. The error suggests the necessity to improve the interpolation accuracy.

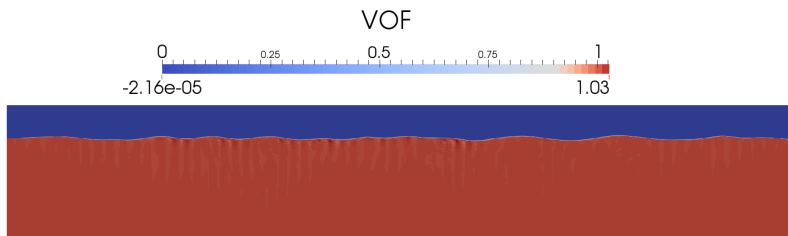


Figure 9: VOF field convected by the irregular wave field interpolated from the HOS method after one peak period. The unbounded VOF field suggests the necessity to improve the interpolation accuracy.

postprocessing stage. The method takes any HOS simulation result as input and allows to refine the grid to a user-defined level.

This refinement is achieved with a zero-padding step in the spectral domain before the IFFT (see Fig. 10). After reading the amplitudes of Fourier components from an HOS result, the method extends the spectrum by adding extra modes with zero amplitude at the end. According to the relation between the spectral and the spatial domain in the FFT algorithm, additional Fourier components result in extra spatial points, i.e., if the spectrum is extended n times, the distance between two HOS points can be reduced to $1/n$. Note that the factor n has to be an integer to end up with the original spatial points plus $n - 1$ additional points between two original points. In this way, the incident result is available on a finer grid and the interpolation error is reduced consequently. Although more points are added, the efficiency is still greatly enhanced compared to the analytical evaluation, since this method still relies on the IFFT.

To demonstrate the improvement in the interpolation accuracy, the divergence of the HOS velocity reconstructed by the zero-padding method is shown in Fig. 11. The same CFD mesh and the same HOS simulation results are used as in Fig. 8. The zero-padding method transfers the modal information on 512 reconstruction points by extending the Fourier modes by a factor of 4. Compared to Fig. 8 the divergence error is reduced by 2 orders of magnitudes. This level of accuracy appears to be enough in our experience to convect the VOF field in a stable way (compare Fig. 12 to Fig. 9).

3.2.5 Code availability

This reconstruction technique is included in the open-source library *Grid2Grid* [1, 19]. This library is developed by the LHEEA research department (Ecole Centrale Nantes and CNRS) to connect any CFD solver with *HOS-Ocean* [28, 40] and *HOS-NWT* [2, 27], two open-source HOS wave solvers. The library

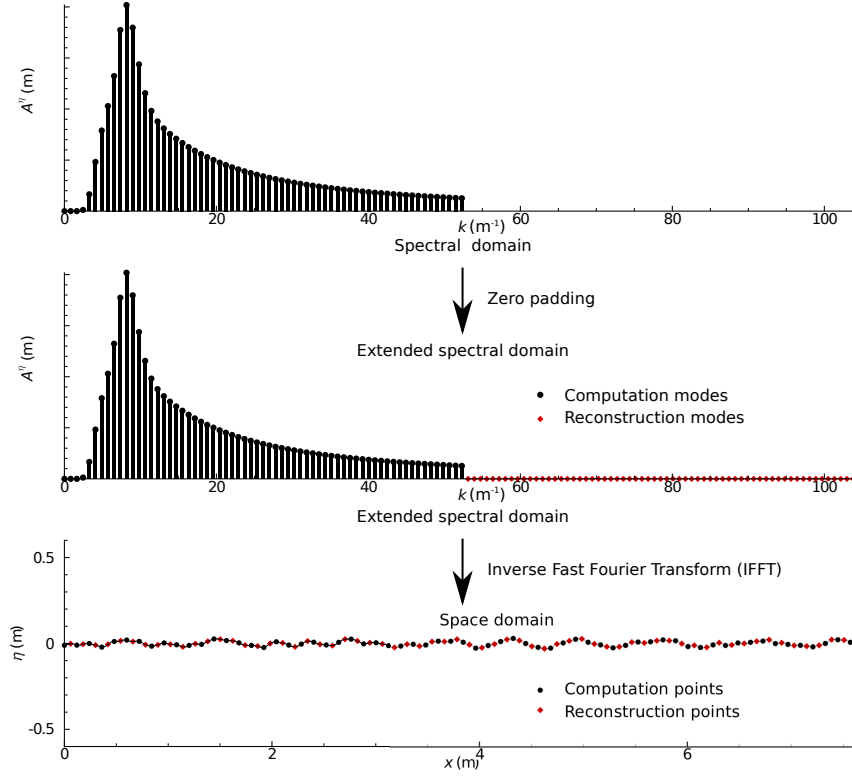


Figure 10: Zero-padding procedure for increasing the spatial resolution of the HOS results. The original spectrum of the HOS solution (on the top) is extended by adding extra modes of zero amplitude at the end (in the middle). It results in extra points in the space domain, and thus the HOS grid is refined.

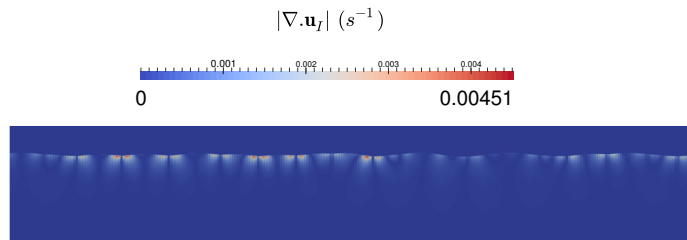


Figure 11: Divergence error of an interpolated HOS velocity field on a CFD mesh with the zero-padding improvement: HOS grid refined with a factor of 4.

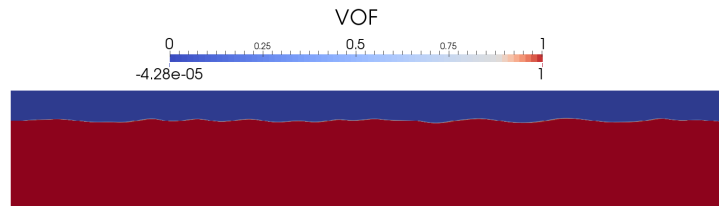


Figure 12: VOF field convected by the irregular wave field interpolated from the HOS method after one peak period with the zero-padding improvement: HOS grid refined with a factor of 4.

is published with the GNU General Public License v3.0 and can be downloaded from the url: <https://github.com/LHEEA/Grid2Grid>.

3.3 Extension of incident wave solution in the air

The two-phase SWENSE method requires the incident solution both in water and in air. However, the wave model only defines the incident solution under the incident free surface position. To obtain the information above the free surface, the incident solution is extended by using Eqn. (39), which gives an incident “solution” even above the free surface. Fig. 13 gives an example of the extended velocity field of a regular wave. The white line represents the free surface position of the incident wave. It is worth noting that the extended solution still satisfies the Euler equations (Eqn. 8 and 9). This property of the spectral method helps the SWENSE method to adjust the definition zone of the incident wave, so that the same functional decomposition can be used in the entire CFD computational domain.

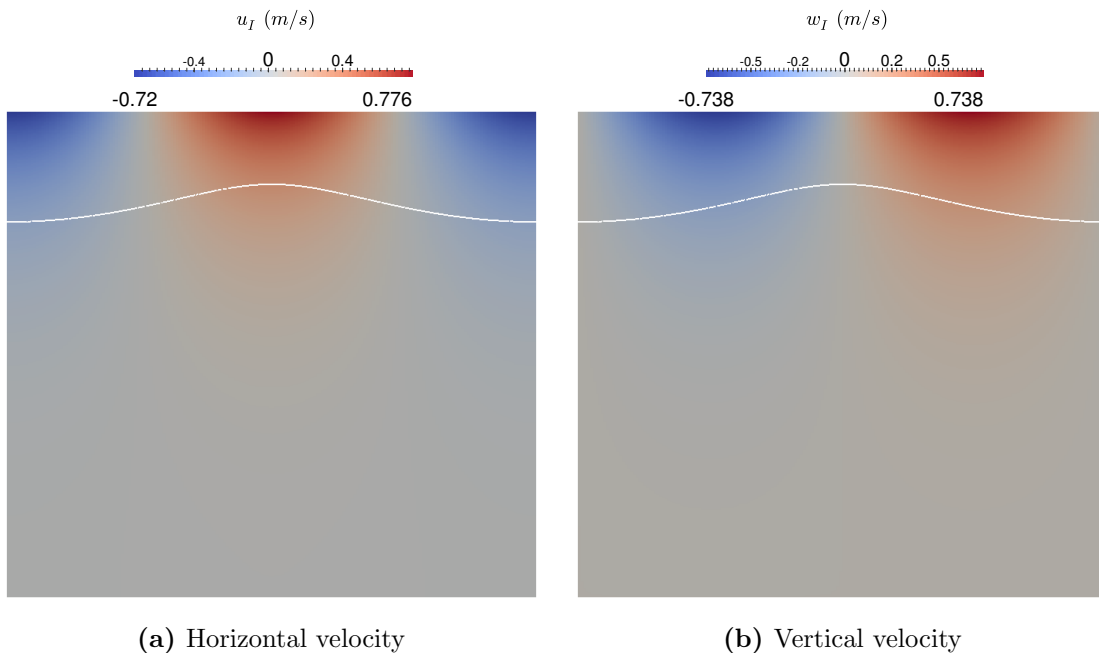


Figure 13: Extended velocity field calculated by the stream function wave theory. The incident free surface is represented by the white line. ($T = 0.7s, H = 0.06m, h = 0.6m$)

This direct extension results in a smooth transition across the free surface, which is beneficial numerically. The drawback of such an extension is an oscillating “*incident wind*” field in the air. By using the boundary conditions given in Tab. 1, this oscillatory wind remains in the total field. Although it is possible to correct this unrealistic phenomenon, (for example, by using no-slip BC on the top), such correction requires extra computational cost in the air, which goes against the objective to reduce CPU time. In the present work, we accept this oscillatory wind as a side effect of the SWENSE decomposition in the air, without any special treatment, since in most classical wave-structure interaction problems, the air-effects are often very weak, as it will be verified in Sect. 5.

4 Implementation in OpenFOAM

The present work uses the open-source CFD package OpenFOAM¹ to implement the proposed method. OpenFOAM uses the second-order Finite Volume method (FVM) with unstructured polyhedral meshes. All the variables are located at the cell center. Its native two-phase solver, *interFoam*, adopts the VOF method [43] and the Multi-Dimensional Limiter for Explicit Solution (MULES) algorithm [23]. The PIMPLE algorithm [67], which combines the Pressure Implicit with Splitting of Operator (PISO) and the Semi-Implicit Method for Pressure-Linked Equations (SIMPLE) [86], is used to obtain converged results of the velocity-pressure-VOF coupling at each time step. The readers are referred to [23, 85] for more details of *interFoam*. The marine hydrodynamics community of OpenFOAM has developed codes based on *interFoam* by adding wave modeling techniques, *e.g.*, *waves2Foam* [47], *foamStar* [64], *etc.*

The proposed two-phase SWENSE method is implemented on top of *foamStar* [64] developed by Bureau Veritas and Ecole Centrale Nantes. The new solver is named as *foamStar-SWENSE*. The only difference between the two solvers is that the NS equations in *foamStar* are replaced by the SWENS equations in *foamStar-SWENSE*.

4.1 Equations discretization

This section briefly describes how the governing equations are discretized. Standard schemes in OpenFOAM are used, as listed in the end of the section. More details of these schemes can be found in the literature [38, 65].

For convenience, the sign $[\cdot]$ is used to indicate that the terms enclosed are treated implicitly. Otherwise, the terms are evaluated explicitly.

4.1.1 VOF equation

The discretization of Eqn. (2) is standard as in *interFoam*:

$$\left[\frac{\partial \alpha}{\partial t} \right] + [\nabla \cdot (\mathbf{u} \alpha)] + \nabla \cdot (\alpha(1 - \alpha) \mathbf{u}_r) = 0 \quad (47)$$

The MULES algorithm [23] is used to keep the boundedness of the α field.

4.1.2 Momentum equation

Eqn. (21), rewritten in its conservative form, is discretized as follows:

$$\left[\frac{\partial \mathbf{u}_C}{\partial t} \right] + [\nabla \cdot (\mathbf{u} \otimes \mathbf{u}_C)] + \nabla \cdot (\mathbf{u}_C \otimes \mathbf{u}_I) - \frac{[\nabla \cdot (\mu_{eff} \nabla \mathbf{u}_C)] + (\nabla \cdot (\mu_{eff} \nabla \mathbf{u}_C))^T}{\rho} = -\frac{\nabla p_C}{\rho} - \frac{p_I}{\rho_I} \frac{\nabla \rho}{\rho} \quad (48)$$

where $\mu_{eff} = \mu + \mu_t$. The time derivative, the convection, and the diffusion terms of the \mathbf{u}_C are discretized implicitly. The rest terms are explicitly evaluated.

Note that the R.H.S. terms are evaluated with a reconstruction operation from face flux [5, 6], to introduce a pseudo-staggered grid setup and to avoid checker-board pressure oscillations that may occur on co-located grids. For example, $\frac{\nabla p_C}{\rho}$ is evaluated at the cell face $\frac{(\nabla p_C)_f}{\rho_f}$ and reconstructed to the cell

¹<https://openfoam.org/>

center. The pressure $(\nabla p_C)_f$ at the cell face is directly calculated with the pressure at the two neighbor cell centers. The face density ρ_f is interpolated as:

$$\rho_f = \frac{\rho_w |\Delta x_w| + \rho_a |\Delta x_a|}{|\Delta x_w + \Delta x_a|} \quad (49)$$

where $|\Delta x_w|$ and $|\Delta x_a|$ denote the distance of cell center to the interface of water cell and air cell respectively. This interpolation scheme mimics the Ghost Fluid Method for two-phase incompressible flow [51]. $\frac{p_I}{\rho_I} \frac{\nabla \rho}{\rho}$ is evaluated similarly.

Eqn. (48), written in a semi-discretized form for a cell P reads:

$$a_P \mathbf{u}_{C,P} + \sum_N a_N \mathbf{u}_{C,N} = \mathbf{S} - \frac{\nabla p_C}{\rho} - \frac{p_I}{\rho_I} \frac{\nabla \rho}{\rho} \quad (50)$$

where the subscript P and N represent the value of the current cell and the values of its neighbors. The coefficients of the discretized system are a_P and a_N . \mathbf{S} represents the source terms in the discretized equation except for the complementary pressure term and the interface term.

In OpenFOAM, the solution step of Eqn. (50) is called the momentum prediction. It provides a momentum conserving velocity field \mathbf{u}_C . However, the result of the velocity prediction does not guarantee the incompressibility of the field. A correction is necessary via the pressure equation step.

4.1.3 Pressure equation

The discretized pressure equation in the SWENSE solver is derived in the same way in as in standard incompressible flow OpenFOAM solvers. The semi-discretized form of the momentum equation Eqn. 50, as follows,

$$a_P \mathbf{u}_{C,P} = H(\mathbf{u}_C) - \frac{\nabla p_C}{\rho} - \frac{p_I}{\rho_I} \frac{\nabla \rho}{\rho} \quad (51)$$

where

- $a_P \mathbf{u}_{C,P}$ is the diagonal contribution of Eqn. (50),
- $-\frac{\nabla p_C}{\rho}$ is the contribution of the complementary pressure gradient,
- $-\frac{p_I}{\rho_I} \frac{\nabla \rho}{\rho}$ is the contribution of interface density gradient,
- $H(\mathbf{u}_{C,P})$ is the off-diagonal contribution of the matrix and the source terms \mathbf{S} in Eqn. (50):

$$H(\mathbf{u}_C) = - \sum_N a_N \mathbf{u}_{C,N} + \mathbf{S} \quad (52)$$

From Eqn. (51)), the complementary velocity at the center of the cell is:

$$\mathbf{u}_{C,P} = \frac{H(\mathbf{u}_C)}{a_P} - \frac{1}{a_P} \frac{\nabla p_C}{\rho} - \frac{1}{a_P} \frac{p_I}{\rho_I} \frac{\nabla \rho}{\rho} \quad (53)$$

Interpolating this value to the face center, yields:

$$\mathbf{u}_{C,f} = \overline{\mathbf{u}_C} = \overline{\left(\frac{H(\mathbf{u}_C)}{a_P} \right)} - \overline{\left(\frac{1}{a_P} \right)} \frac{(\nabla p_C)_f}{\rho_f} - \overline{\left(\frac{1}{a_P} \right)} \frac{p_{I,f}}{\rho_I} \frac{(\nabla \rho)_f}{\rho_f} \quad (54)$$

where the $\bar{\cdot}$ symbol denotes the value on the cell face, which is linearly interpolated from the cell center of both sides.

Substituting Eqn. (54) into Eqn. (14), the discretized pressure equation is written as:

$$\left[\nabla \cdot \left(\overline{\left(\frac{1}{a_P} \right)} \frac{(\nabla p_C)_f}{\rho_f} \right) \right] = \nabla \cdot \left(\overline{\left(\frac{H(\mathbf{u}_C)}{a_p} \right)} - \overline{\left(\frac{1}{a_P} \right)} \frac{p_{I,f}}{\rho_I} \frac{(\nabla \rho)_f}{\rho_f} \right) \quad (55)$$

This Poisson equation is used to determine the complementary pressure field and to correct the complementary velocity flux. At last, the flux is used to reconstruct the cell-centered \mathbf{u}_C .

4.1.4 Discretization Schemes

The discretization schemes are listed in Tab. 2. The time derivative is discretized with second-order Crank-Nicolson scheme and blended with first-order Euler implicit scheme to compromise between the accuracy and the stability. Spatial schemes are also 2nd-order in general, but first-order schemes will be used locally to avoid over-shoots (or under-shoots).

Table 2: The discretization schemes in foamStar-SWENSE

	Term	Discretization scheme
Time derivative	default	Crank Nicolson (2nd-order) blended with Euler Implicit (1st-order)
Gradient	default	cellLimited leastSquares (2nd-order with 1st order limiter)
	$\nabla \alpha$	Gauss linear (2nd-order)
Divergence	default	Gauss linear (2nd-order)
	$\nabla \cdot (\mathbf{u} \otimes \mathbf{u}_C)$	Gauss linearUpwindV (2nd-order with 1st-order limiter)
	$\nabla \cdot (\mathbf{u}\alpha)$	Gauss vanLeer01 (2nd-order with 1st-order limiter)
Laplacian	default	Gauss linear limited correct 0.5 (2nd-order with 1st-order limiter)
Interpolation	default	linear (2nd-order)
	$\rho_{c \rightarrow f}$	linear and interface density interpolation (Eqn. (49)) (2nd-order)
Surface normal gradient	default	limited corrected 0.5 (2nd-order with 1st-order limiter)

4.2 Prevention of wave reflections with the relaxation zone technique

A relaxation zone technique is used to prevent wave reflections at the computational domain boundaries. It defines regions where the computed value is gradually blended to the target value using a space-dependent weight function ω as shown in Fig. 14. For a given quantity χ , the relaxed value χ_{relax} in these regions is defined as the linear combination of the numerical solution χ_{CFD} and the target value χ_{target} , as follows:

$$\chi_{relax} = \omega \chi_{target} + (1 - \omega) \chi_{CFD} \quad (56)$$

This relaxation step is applied at the end of each time step after the solution of CFD solver has converged. The relaxed value is then used in the further simulation.

The weight function is defined in a way such that it is equal to 1 on the boundary and 0 in the full CFD domain. The present implementation follows reference [64]. The weight function reads,

$$\omega = -2x^3 + 3x^2 \quad (57)$$

where x is the non-dimensional distance to the inner boundary of the relaxation zone. $x = 1$ corresponds to the outer boundary of the relaxation zone. $x = 0$ corresponds to the interface between the pure CFD and the relaxation zone.

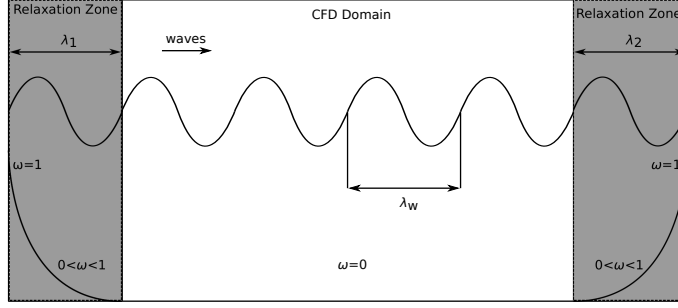


Figure 14: Relaxation zone technique principle

In the relaxation zones, the complementary velocity field \mathbf{u}_C is gradually attenuated to zero, and the VOF field α is blended to the target value of incident wave field α_I , as follows:

$$\mathbf{u}_{C,relax} = \omega \mathbf{0} + (1 - \omega) \mathbf{u}_{C,CFD} \quad (58)$$

$$\alpha_{relax} = \omega \alpha_I + (1 - \omega) \alpha_{CFD} \quad (59)$$

since the SWENSE method assumes that the complementary waves vanish in the far-field. The pressure is not relaxed by this method as it is solved implicitly at each step.

4.3 Solution algorithm

The structure of the SWENSE solver is provided in the flowchart of Fig. 15.

1. At the beginning of each time step, incident wave properties \mathbf{u}_I and p_I are updated from potential wave solvers and mapped on the CFD mesh. The total velocity is reconstructed with $\mathbf{u} = \mathbf{u}_I + \mathbf{u}_C$.
2. Solve for the VOF field α (Eqn. 47); update the fluid properties with the new VOF field (Eqn. 3 and 4). Update the modified incident wave pressure (p_I^*) with the new density field (Eqn. 15).
3. In the PISO loop, the complementary velocity field is solved from Eqn. (48) at first (the momentum prediction step). Secondly, the complementary pressure p_C is solved from Eqn. (55). The flux of the complementary velocity is corrected by the pressure field p_C . After the correction, the flux is used to reconstruct the complementary velocity field \mathbf{u}_C at the cell center. The PISO loop iterates until reaching the maximum iteration number (user defined value, set to 6 in the present cases).
4. The solution is then blended to the target values in the relaxation zones to attenuate the complementary waves in the far-field (Eqns. 58 and 59)
5. Outer nonlinear iterations are made to achieve the convergence of the VOF, the velocity, and the pressure before stepping to the next time. The convergence criterion is that the residual of \mathbf{u}_C is reduced 3 orders of magnitude.

5 Validation and Application

In this section, the two-phase SWENSE method is validated on three test cases:

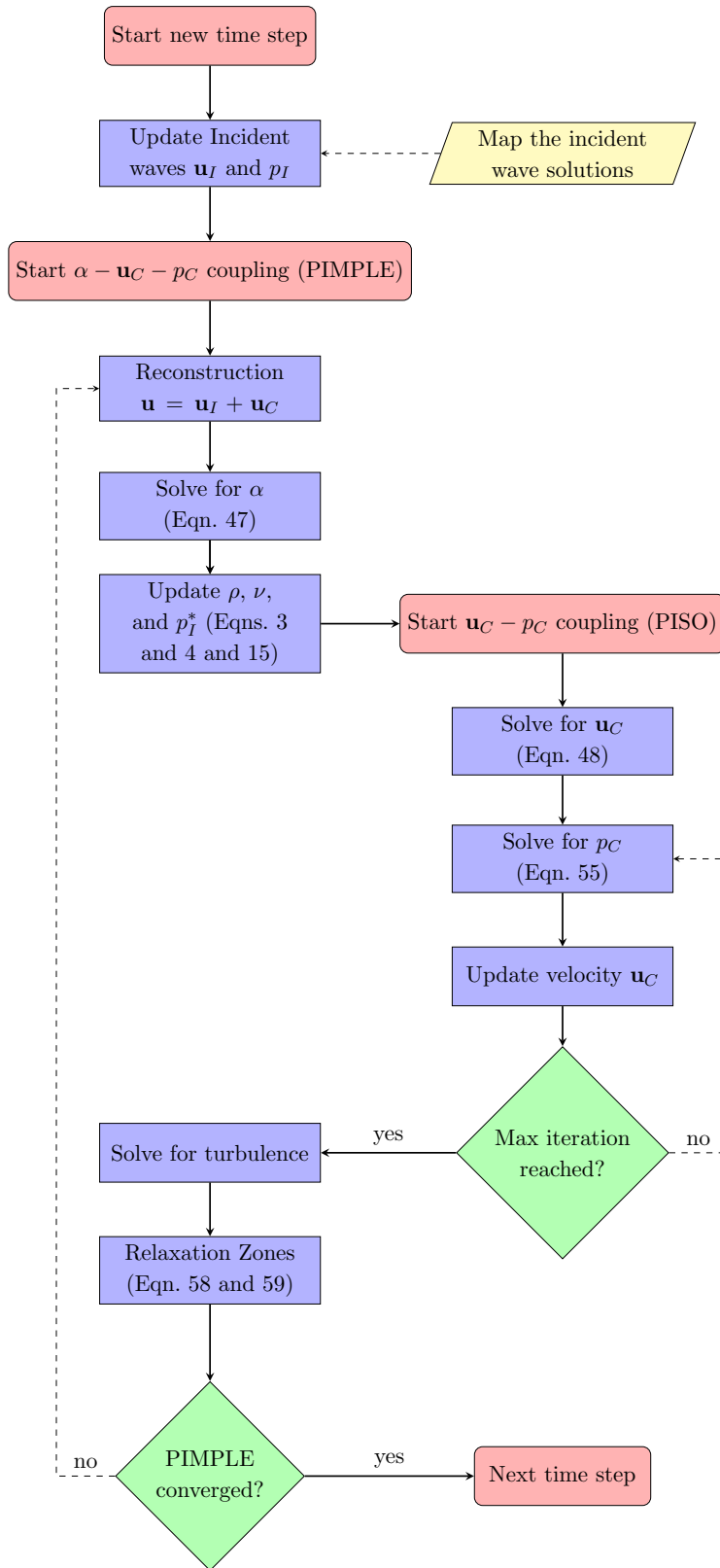


Figure 15: Solution algorithm of the SWENSE method

- Progressive waves: This test case consists simply in a simple regular wave propagation in a periodic domain. No structure is present. Different discretizations are used to check whether a SWENSE solver can keep incident waves accurate with coarse discretizations. A comparison with the conventional NS solver *foamStar* is also provided.
- High-order wave loads on a vertical cylinder: This case validates the method on the calculation of the wave force on a fixed structure with simple geometry. The horizontal wave force on the cylinder is recorded. Up to fourth harmonic components are extracted and compared with experimental data and numerical results of potential flow solvers. A systematic convergence study is also conducted.
- Fixed Catenary Anchored Leg Mooring (CALM) buoy with a heave-damping skirt in regular and irregular waves: This configuration is used to assess the method with a complex geometry and includes violent free surface deformation and viscous effects representing a real ocean engineering application. The results of *foamStar-SWENSE* are compared with experimental data. For the regular wave case, comparative simulations conducted with *foamStar* are used to demonstrate the efficiency and accuracy of the proposed method.

5.1 Progressive waves

Good quality of the incident waves is the first requirement for wave-structure interaction simulations. NS solvers (e.g., *foamStar*), which simulate the wave system with a direct method, need fine meshes to propagate waves accurately. Instead, incident wave propagation in SWENSE solvers is much easier because the incident waves are explicitly given by wave models. In a SWENSE solver, maintaining the accurate incident waves is nothing more than keeping the complementary field is equal to zero. Although such a property of the proposed two-phase SWENSE method has been demonstrated theoretically in Sect. 2.4, numerical errors may exist in CFD simulations. Therefore, this case tests the real behavior of *foamStar-SWENSE*, taking all the probable numerical errors into account.

The case simulates regular wave propagation in a 2D periodic domain. Periodic boundary conditions at inlet and outlet are used to get rid of the wave generation and absorption issues and to focus on the wave propagation. The case is intentionally designed with a large computational domain and a long time duration to increase the numerical errors, in order to test the stability and the accuracy of the method.

foamStar-SWENSE and *foamStar* are tested and compared with several identical spatial and temporal discretizations.

5.1.1 Test case setup

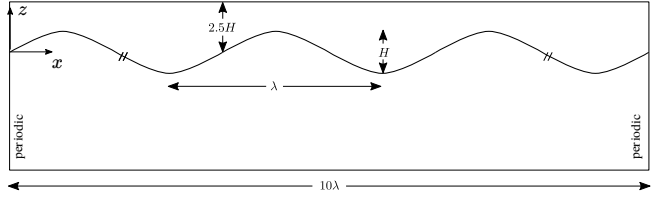
Regular waves with a moderately large wave steepness ($ka = 0.22$) are simulated. The wave characteristics are listed in Tab. 3. The stream function wave theory [30, 73] is used to generate the reference solution and provide the incident wave information to *foamStar-SWENSE*.

The simulations use a two-dimensional rectangular computational domain (see Fig. 16). The waves travel from the left to the right. Periodic boundary conditions are applied on the left and the right boundaries. The origin of the coordinate system is located at the left of the computational domain on the free surface position at rest. The axis x points right and the axis z points up. The length of the computational domain is equal to ten wave lengths (λ), and the height of the computational domain is equal to the water depth (h) plus 2.5 times the wave height (H). The simulation time is equal to 20 wave periods.

Three sets of space and time resolutions are used (see Tab. 4). The medium discretization corresponds to the typical mesh used by two-phase VOF solvers for the wave-structure interaction problems.

Table 3: Progressive wave test case: wave parameters

Parameter	Value
Wave period (T)	0.70 s
Wave height ($H = 2a$)	0.058 m
Water depth (h)	0.60 m
Wave steepness (ka)	0.22
Relative water depth (kh)	4.7

**Figure 16:** Progressive waves test case: computational domain**Table 4:** Progressive waves test case: numerical resolutions

Parameter	Coarse	Medium	Fine
Mesh size ($\Delta x, \Delta z$)	$\lambda/50, H/10$	$\lambda/100, H/20$	$\lambda/200, H/40$
Time step (Δt)	$T/200$	$T/400$	$T/800$

For *foamStar-SWENSE*, the initial values of the complementary velocity field \mathbf{u}_C and the complementary pressure field p_C are set to zero; the VOF field is set according to the stream function wave theory. For *foamStar*, the initial values of the velocity field \mathbf{u} , pressure field p_d , and the VOF field α are set according to the stream function wave theory.

5.1.2 Numerical results

The free surface elevation at the center of the domain is measured. Figure 17 plots the time evolution of the first and second harmonics. The vertical axis is normalized by the reference stream function value; the horizontal axis is non-dimensionalized by the wave period. The errors on the first harmonic are listed in Tab. 5 every five periods.

foamStar-SWENSE: Figure 17 reveals that the first and the second harmonic amplitudes are well kept for the entire 20 wave periods, with all the three discretizations. The fine and the medium discretizations give very close results; the coarse discretization produces results with slightly larger errors, but still simulates the waves rather accurately. Tab. 5 confirms the above observations. The three meshes have relative errors of 2.45%, 0.81%, and 1.03% at $t = 20T$.

foamStar: Figure 17 suggests a more remarkable wave damping throughout the 20 periods with all the discretizations. The loss of wave amplitude is of 18.97%, 6.68% and 2.45% for the coarse, medium and fine meshes at $t = 20T$.

Table 5: Progressive waves test case: Relative errors on the first harmonic amplitude of the free surface elevation at the center of the computational domain

		5T	10T	15T	20T
<i>foamStar-SWENSE</i>	coarse	1.11%	1.61%	1.80%	2.45%
	medium	0.27%	0.47%	0.53%	0.81%
	fine	0.17%	0.38%	0.66%	1.03%
<i>foamStar</i>	coarse	4.10%	9.89%	14.50%	18.97%
	medium	1.30%	3.33%	4.90%	6.68%
	fine	0.44%	1.19%	1.75%	2.45%

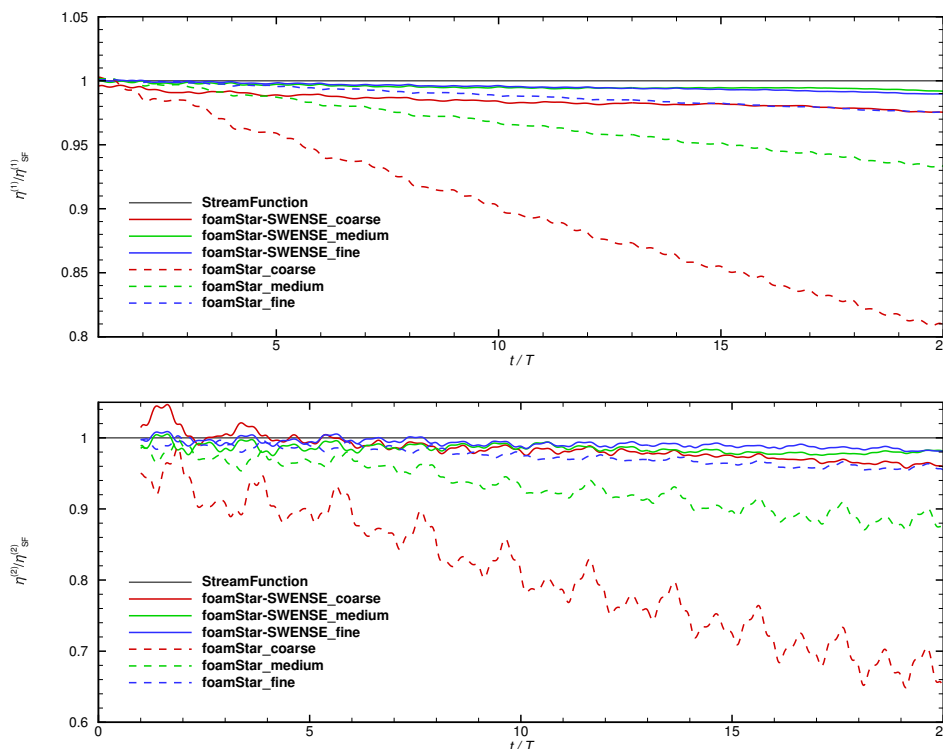


Figure 17: Progressive waves test case: Harmonic amplitudes of the free surface elevation at the center of the domain. Top plot: first harmonic amplitude. Bottom plot: second harmonic amplitude.

5.1.3 Discussion

Numerical errors in two-phase SWENSE method

Although Sect. 2.4.2 proves that the SWENSE method keeps the waves equal to the incident solution in theory, the simulation results show a difference. One reason for this contradiction is the error created when approximating the interface position by the contour of $\alpha = 0.5$. Theoretically, the complementary fields are kept zero in a pure incident wave propagation case because the free surface position (the density jump) coincides with the $p_I = 0$ contour (incident free surface position). However, the present implementation defines the density jump at $\alpha = 0.5$, where p_I is slightly different from 0. An error in $\frac{p_I}{\rho_I} \frac{\nabla \rho}{\rho}$ of the

momentum equation (Eqn. 21) is introduced and generates a tiny spurious complementary field near the free surface. Even with refinement, this error cannot be fully reduced to zero. In the future, better definition of the density jump can be considered with more advanced interface capturing methods to improve the result. For now, we satisfy with the method since it provides more accurate results than the NS solver, as shown below.

Advantage in keeping incident waves over conventional solvers

In Fig. 17, the results of *foamStar* show the well known numerical wave damping problem of two-phase NS solvers [18, 63] and the wave damping is more severe with coarser discretizations. For this reason, the International Towing Tank Conference (ITTC) suggests more than 80 grids per wavelength when using 2nd-order CFD codes for wave problems [46]. For *foamStar-SWENSE*, the results are very close to the reference value, even with the coarse discretization. Moreover, *foamStar-SWENSE* with the coarse mesh gives results as good as *foamStar* with the fine mesh, showing that *foamStar* needs 4 times more refined discretization to achieve the same accuracy. An obvious efficiency gain of the SWENSE method is confirmed.

5.2 High-order wave forces on a vertical cylinder

High-order wave force on cylinders is a classical problem in offshore engineering. Despite their small amplitudes, the high-order wave forces may cause sudden structural vibration (the so-called “ringing” phenomenon), since their frequencies are close to the natural frequency of the structure. This problem has been addressed by numerous approaches in the literature, including asymptotic analytical solutions [33, 58], experiment [44], and numerical simulations with fully nonlinear potential flow approaches [34, 81]. Therefore, these well-established reference data make this case very suitable for validation purposes.

The test case contains two following parts:

- A convergence study in a rather steep wave condition ($ka = 0.24$).
- Validation of the method with simulations covering eight different wave steepnesses ($0.6 < ka < 0.24$).

5.2.1 Test case setup

The simulation reproduces the experiment in [44], where a thin cylinder is exposed to regular waves in deep water (see Fig. 18). The cylinder has a radius of $R = 0.03$ m, being fixed in the water tank of water depth $h = 0.6$ m. The incident wave frequency f is equal to 1.425 Hz. Different wave amplitudes (a) are used in the experiment and the data are available for a series of wave steepnesses in the range of $ka \in [0.03, 0.24]$.

For convenience, a cylindrical mesh is used by the simulation, instead of modeling the entire experimental wave tank (see Fig. 19). The cylinder is located at the center. At far-field, the complementary field is damped to avoid reflections. This configuration represents an ideal experimental condition, where no wave reflects back from the boundaries. This kind of mesh is also used by the potential flow solvers producing the reference data [34, 81].

The cylindrical mesh is also accurate and efficient for the SWENSE method: The mesh is fine near the center, which helps to capture the complementary fields accurately near the structure; Coarse mesh in the far-field helps to reduce the computational cost. Please note that NS solvers cannot use such a mesh, since coarse far-field mesh results in inaccurate incident waves.

A longitudinal symmetry plane is used. The origin of the coordinate system coincides with the cylinder’s center-line and is located at the still water level, axis x points to the incident wave propagation direction

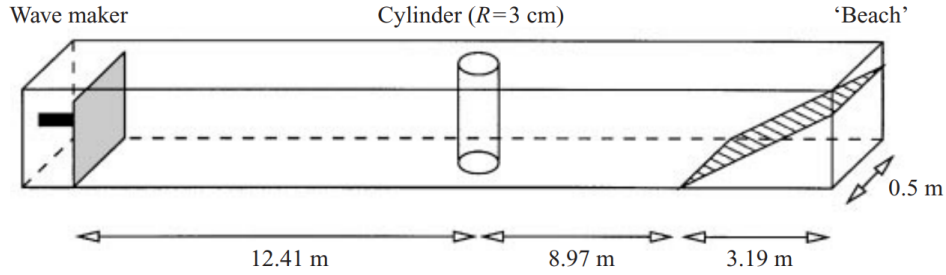


Figure 18: High-order wave forces test case: The experiment setup [44]. Reprinted with permission, copyright Cambridge University Press.

and axis z points upward. Along z axis, the computational domain extends from the tank bottom at $z = -h$ until $z = 5a$ in the air. In z direction, the mesh is uniform near the air-water interface $z \in (-1.5a, 1.5a)$. The cell size increases gradually out of this refined zone. The domains radius is equal to 2 wave lengths ($L_r = 2\lambda$). The mesh is refined near the cylinder and gradually enlarged along the radius direction. In the far-field, a relaxation zone with a length of $L_{relax} = 1.5\lambda$ is used to absorb the complementary field, leaving a pure CFD zone with one wave length diameter. The setup of the relaxation zone follows the study in [68], which shows a relaxation zone of at least 1λ long locating at least $1/6\lambda$ away from the structure is sufficient. The setup is summarized in Tab. 6.

The maximum Reynolds number $Re = 1.55 \times 10^4$ when the wave crest reaches the cylinder, indicating the flow is between the laminar and transitional regime with a Keulegan-Carpenter number $KC = 3.01$. As a result, no turbulence model is used. No-slip wall boundary condition is applied on the cylinder with under-resolved boundary layer. It is acceptable since the viscous force is very small compared to the pressure contribution.

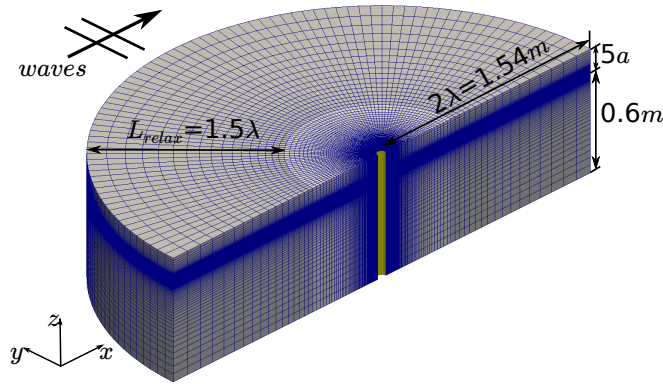


Figure 19: High-order wave forces test case: Cylindrical mesh used for the simulations

5.2.2 Convergence study

A systematic convergence study with six sets of temporal and spatial resolutions is conducted. The time step and the mesh size—in radial, tangential, and vertical directions—are changed simultaneously. The discretization details are summarized in Tab. 7. This study uses the steepest wave case ($ka = 0.24$) in the

Table 6: Parameters for test case cylinder in waves

Parameter	Value
Cylinder radius (R)	0.03 m
Water depth (h)	0.60 m
Wave frequency (f)	1.425 Hz
Domain size ($L_r \times L_\theta \times L_z$)	$2\lambda \times 180^\circ \times (h + 5a)$
Relaxation Zone Length (L_{relax})	1.5λ

experiment.

Table 7: High-order wave forces test case: Spatial and temporal resolutions for the convergence study

Index	Number of cells in				Time step $T/\Delta t$
	radial direction	tangential direction	a wave amplitude	total	
1	50	40	6	88,000	200
2	60	48	7	155,520	240
3	71	56	9	246,512	285
4	100	80	12	668,000	400
5	140	112	17	1,881,600	560
6	200	160	24	5,504,000	800

Figure 20 shows the time histories of the inline force obtained with different discretizations. The abscissa denotes the time t , which is normalized by the wave period T . It is observed that a periodic regime appears after two wave periods. The bottom plot zooms in between the fourth and fifth periods. The first observation is that the results are very close and converge with the refinement.

For a better comparison, the time histories in the periodic regime are transformed to the frequency domain by the Fast Fourier Transform (FFT). The amplitudes of the first four harmonic components are summarized in Tab. 8. Following [44], the harmonic amplitudes in the table are normalized using:

$$F'_n = \frac{F_n}{\rho g R^3} \left(\frac{R}{a} \right)^n \quad (60)$$

Table 8: High-order wave forces test case: Harmonic amplitudes of inline wave force obtained with different mesh resolutions

Harmonic amplitude	Mesh					
	1	2	3	4	5	6
F'_1	6.029	6.142	6.198	6.299	6.366	6.403
F'_2	0.225	0.223	0.210	0.210	0.205	0.207
F'_3	0.207	0.219	0.229	0.241	0.247	0.243
F'_4	0.111	0.118	0.121	0.124	0.125	0.125

Figure 21 shows the variation of the normalized harmonic amplitudes with the mesh refinement. The abscissa represents the mesh 1 to 6 and is scaled by the number of cells per dimension. Again, it is observed

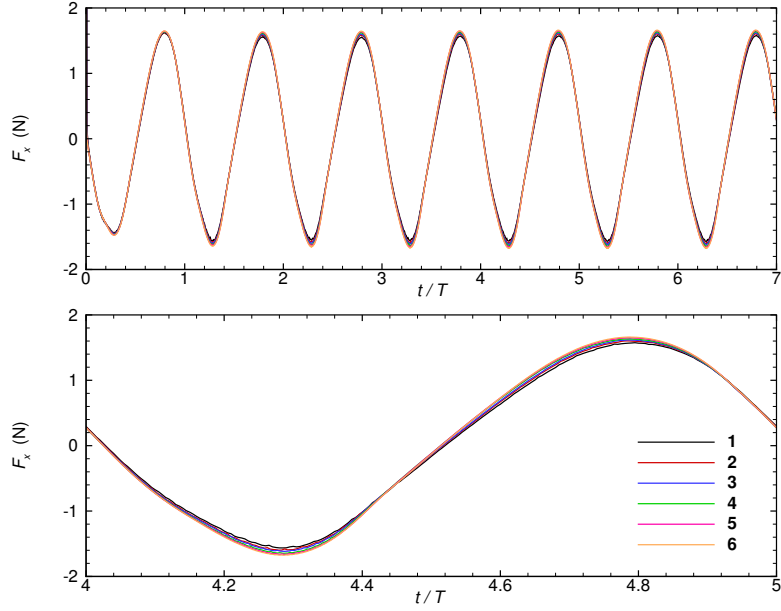


Figure 20: High-order wave forces test case: Time history of the inline wave force with different mesh resolutions

that results with different discretizations are very close, showing that even the coarsest mesh can give a good prediction of force.

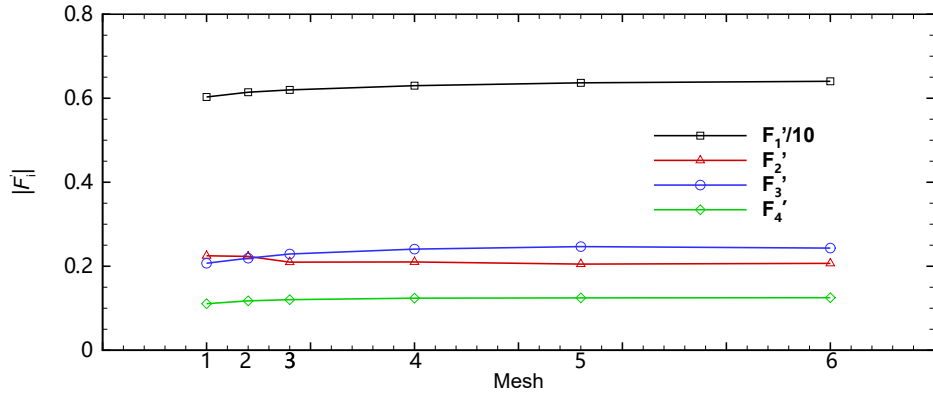


Figure 21: High-order wave forces test case: Harmonic amplitudes of the inline wave force obtained with different mesh resolutions.

In the following, the error estimation procedure proposed by [31] is adopted to estimate the convergence rate and the converged value. This procedure assumes that the discretization error is a power function of the mesh and time-step size, as follows:

$$\epsilon_i = \phi_i - \phi_0 = \alpha(\Delta x)^{p_x} + \beta(\Delta t)^{p_t} \quad (61)$$

where ϵ_i is the discretization error of the simulation result ϕ_i , while ϕ_0 denotes the extrapolated “exact” solution of the mathematical equations. Δx and Δt stand for the characteristic mesh and time-step size. p_x

and p_t are the convergence order in space and time. For each harmonic amplitude, the five parameters: ϕ_0 , α , p_x , β , p_t are determined by the method of least-squares, using the six discretization results.

The converged values ϕ_0 and the convergence order are listed, in Tab. 9. The results show a general convergence order between 1 and 2, which is coherent with the discretization schemes used in OpenFOAM (second order convective schemes with first order limiters).

Table 9: High-order wave forces test case: Estimated “exact” value and order of convergence for the first to fourth harmonic amplitudes

Harmonic amplitude	“Exact” Value (ϕ_0)	Order of convergence	
		space (p_x)	time (p_t)
F'_1	6.459	1.5	1.5
F'_2	0.204	1.8	1.8
F'_3	0.256	1.6	1.6
F'_4	0.123	1.2	2

Table 10 presents the “relative error” for different mesh resolutions. The “relative error” is defined with the following equation, according to [31].

$$\delta_i = \frac{|\phi_i - \phi_0|}{|\phi_0|}. \quad (62)$$

Table 10: High-order wave forces test case: “Relative errors” for different mesh resolutions

Harmonic amplitude	“Relative errors” for different meshes (%)					
	1	2	3	4	5	6
F'_1	6.66	4.90	4.03	2.48	1.44	0.87
F'_2	10.24	9.51	2.82	3.03	0.54	1.40
F'_3	19.11	14.40	10.51	5.96	3.64	5.02
F'_4	9.89	4.41	2.06	0.74	1.32	1.70

From Tab. 10, it is observed that:

- The first harmonic amplitude is predicted rather accurately even with the coarsest mesh (6.66% error). This should be credited to the advantage of the SWENSE method and the use of an optimal cylindrical mesh. The SWENSE method ensures a good incident wave, allowing the use of coarse mesh in the far-field; the cylindrical mesh is refined near the structure so that it is always fine “enough” to calculate the first harmonic amplitude correctly.
- Higher harmonic components contain larger “relative errors” than that in the first harmonic component, since the high-order components are smaller and thus require finer discretizations to be captured accurately. Even so, the accuracy with the coarsest mesh is still rather satisfying, with a maximum “relative error” smaller than 20%.
- For the finest mesh, errors are so low that the convergence seems to saturate. However, one must remember here that it is a “relative” error to an estimated solution and not to an exact one, so that errors of the order of a few percents do not represent the absolute accuracy of the method.

5.2.3 Steepness study

In this part, the wave force with eight wave steepnesses ($ka \in \{0.06, 0.08, 0.10, 0.13, 0.15, 0.17, 0.20, 0.24\}$) are calculated with *foamStar-SWENSE*. The mesh 4 of the previous section is used, to make a compromise between the computational cost and the accuracy. Table 10 shows that this mesh achieves a rather small “relative errors”, with only 0.67 million cells (1/8 of the finest mesh). The mesh is adjusted in the vertical direction according to the wave steepness so that the number of cells per wave amplitude is the same.

The harmonic amplitudes and the phase shifts calculated by *foamStar-SWENSE* are compared with reference data in Fig. 22. From the top to the bottom, the first to the fourth harmonic components. The amplitudes are shown on the left and the phase shifts are shown on the right. In each subplot, the horizontal axis denotes the wave steepness. The reference data include:

- The third-order analytical solution of Malenica and Molin [58] (referred to as Analytical).
- The experiment data reference [44] (referred to as EXP).
- Two numerical results using fully nonlinear potential flow theory (referred to as Ferrant [35] and Shao *et al.* [81]).

To analyze these results, the primary focus is put on the first harmonic amplitudes (Fig. 22a), since it is dominant. In general, *foamStar-SWENSE* shows a very close agreement with experimental data. This agreement suggests the accuracy of the proposed method in calculating the wave load. When compared with the potential theory results of Ferrant [35] and Shao *et al.* [81], *foamStar-SWENSE* shows also a good agreement at small wave steepness ($ka < 0.1$). For $ka > 0.1$, *foamStar-SWENSE* is more accurate than the potential flow solvers, since the SWENSE method is able to capture the flow separation and violent free surface deformations (see Fig. 23), where PT solvers encounter numerical difficulties [52].

For the second harmonic amplitudes, both *foamStar-SWENSE* and the experiment show the same decreasing trend when the wave steepness becomes larger. The results are approximately 20% larger than the experimental data and are closer to experimental data than that of the potential flow solvers where they are available.

For the third and fourth harmonic amplitudes, the comparison is better when the wave steepness is large. For small wave steepness, it is indeed more difficult because the magnitudes of the high-order force are very small. The oscillations appearing in the experimental data also confirm this difficulty.

For the phase shifts, a good agreement is shown among the analytical solution and all the numerical results, which are, however, different from the experimental data. The reason for this discrepancy is still not clear [81], but it may due to a setup slightly different in the experiment. More specifically, in consideration of the difference getting larger while the order increases, it is possible that the beginning time of the experiment and the calculations are different.

To conclude, this comparison demonstrates that the proposed two-phase SWENSE method is able to calculate the wave force on a simple structure for a large range of wave steepness. The typical cylindrical mesh with coarse cells in the far-field can be used to reduce the computational cost without influencing the accuracy.

5.3 CALM buoy in regular and irregular waves

This part aims to demonstrate the ability of the two-phase SWENSE method in dealing with a more complex geometry and wave conditions.

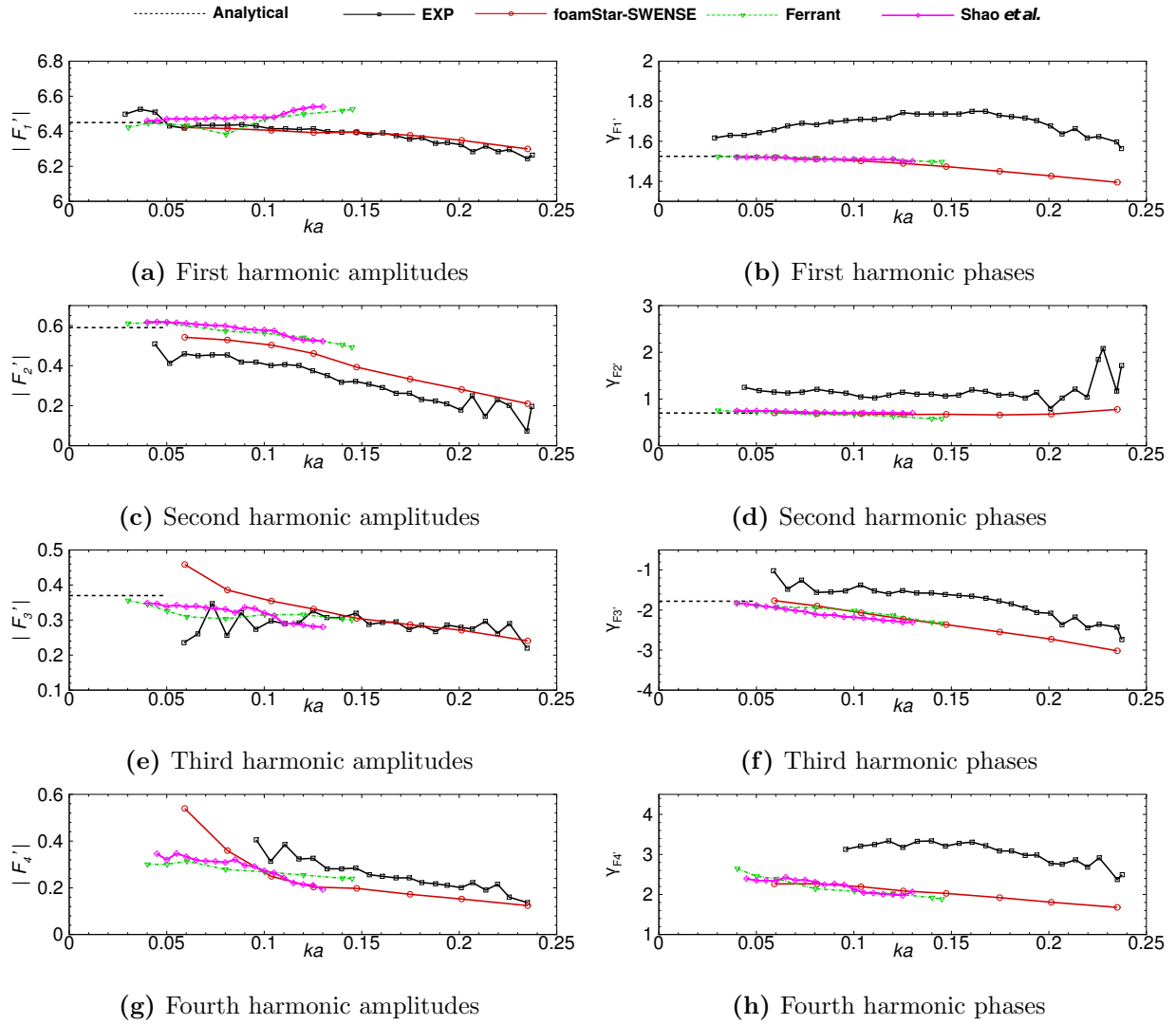


Figure 22: High-order wave forces test case: Comparison of the first to fourth harmonics of horizontal forces on vertical circular cylinder in regular waves with $kR = 0.245$.

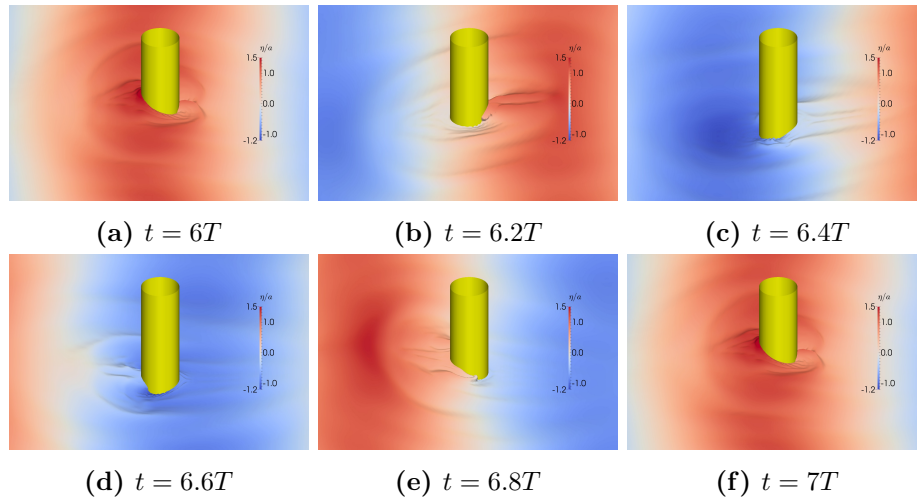


Figure 23: High-order wave forces test case: Free surface near the cylinder (incident wave steepness $ka = 0.24$)

- Geometry: The Catenary Anchor Leg Mooring (CALM) buoy [75] contains a thin heave-damping skirt. Violent free surface deformation and significant flow separation induced by such a geometry needs to be captured by the complementary field.
- Wave condition: Both regular and irregular wave conditions are used. The irregular waves are obtained with *HOS-NWT* solver and reconstructed onto the CFD mesh to validate the reconstruction method proposed in Sect. 3.
- Turbulence modeling: The $k - \omega$ SST turbulence model [61] is used. The non-slip boundary condition is applied on the buoy with standard wall functions in OpenFOAM [54].

In addition, the accuracy and efficiency of *foamStar-SWENSE* and *foamStar* are compared in the regular wave condition. Here the results are shown in a concise version for validation purposes. The interested reader can find details about the regular wave case in a separate paper [53].

5.3.1 Geometry and wave parameters

The test case reproduces an experiment carried out in the ocean engineering basin of Ecole Centrale Nantes (50m long, 30m wide and 5m deep). The buoy is a truncated cylinder with a thin skirt near the bottom to provide additional damping forces through vortex shedding (see Fig. 24a and Tab. 11). The horizontal and vertical wave forces and the free surface elevations at three points are measured (see Fig. 24b).

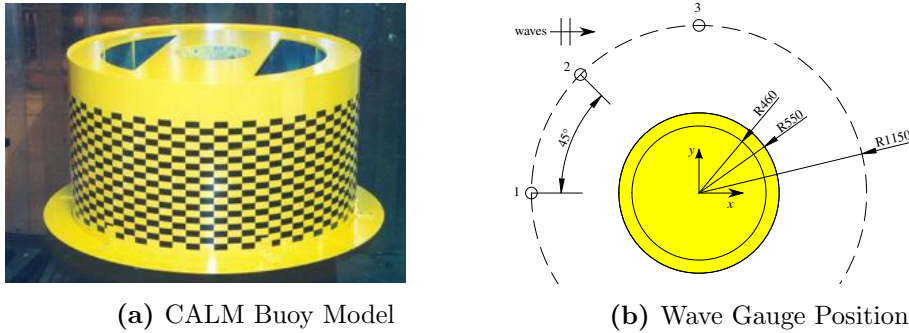


Figure 24: CALM buoy test case: Model geometry and experiment setup

Regular and irregular wave conditions, chosen from the experiment, are listed in Tab. 12. The wave steepnesses are moderate. The irregular waves are generated with a JONSWAP spectrum with $\gamma = 3$.

5.3.2 Computational domain and meshes

A cylindrical and a rectangular mesh configurations are used. The cylindrical mesh is used by *foamStar-SWENSE* in both regular and irregular wave cases. However, the cylindrical mesh is unsuitable for *foamStar*, because the coarse cells in the far-field deteriorate the incident waves. For this reason, a series of rectangular meshes are used in the comparative study by both *foamStar* and *foamStar-SWENSE*. The computational domain is defined with the regular wave's parameter (λ, H).

Cylindrical configuration

The domain radius is equal to 2λ . The depth is equal to that of the experimental wave tank (5m). The top is 0.5m above the free surface position at rest. A longitudinal symmetry plane is used. The cells near

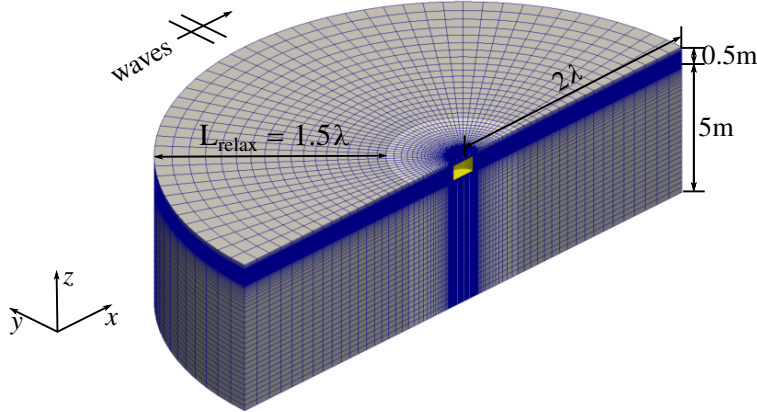
Table 11: CALM buoy test case: Geometry characteristics

Parameter	Value
Radius	0.460 m
Height overall	0.560 m
Skirt radius	0.550 m
Skirt thickness	0.004 m
From the bottom to the mid-skirt	0.04 m
Draft	0.25 m

Table 12: CALM buoy test case: Wave conditions

Regular waves		Irregular waves	
T	1.80 s	T_p	2.00 s
H	0.16 m	H_s	0.12 m
$kH/2$	0.1	$k_p H_s/2$	0.06

the structure are refined in the radial direction to capture the flow details. Cells are gradually enlarged in the far-field (see Fig. 25). The discretization details are listed in Tab. 13. In the far-field, a relaxation zone with a length of 1.5λ is used to absorb the disturbed wave field, leaving a pure CFD zone with one wave length diameter, i.e., $r \in (-0.5\lambda, 0.5\lambda)$. The relaxation zone setup is the same as the cylinder in wave case, following also [68].

**Figure 25:** CALM buoy test case: Cylindrical mesh layout [53]. Reprinted with permission, copyright Elsevier®.

Rectangular configurations

The rectangular configurations use uniform Cartesian background mesh to facilitate the incident wave propagation with *foamStar*. Three configurations: x20, x40, and x80 are used with 20, 40, and 80 cells per wave length in the x direction. The mesh in the transverse direction is less refined than in the x direction to reduce the total number of cells (see Fig. 26). In the far-field, relaxation zones with a length of 1.5λ are set at the inlet, the outlet, and the sides. The mesh details are summarized in Tab. 14.

The local mesh refinement near the structure is invariant for all the three configurations and has a cell

Table 13: CALM buoy test case: Cylindrical mesh information

Parameter	Value
$\lambda/\Delta R_{near}$	400
$\lambda/\Delta R_{far}$	10
$180^\circ/\Delta\theta$	96
$H/\Delta z$	16
Total Cells	0.72 M

density similar to that of the cylindrical configuration. Thus the differences between the x20, x40, x80, and the cylindrical mesh are in the far-field only.

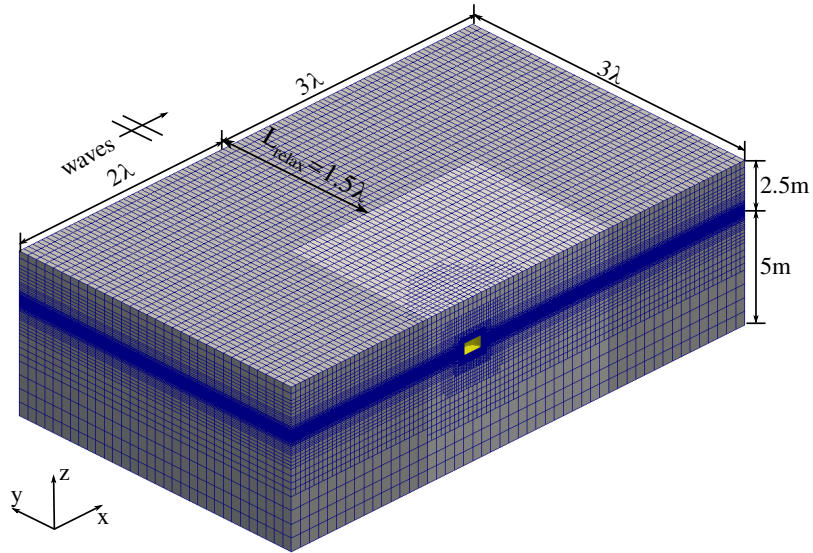


Figure 26: CALM buoy test case: Rectangular mesh layout [53]. Reprinted with permission, copyright Elsevier®.

Table 14: CALM buoy test case: Rectangular mesh information

Mesh	$\lambda/\Delta x$	$\lambda/\Delta y$	$H/\Delta z$	Number of cells
x20	20	10	16	1.28 M
x40	40	10	16	1.47 M
x80	80	20	16	2.58 M

5.3.3 Regular waves

The experimental condition with regular waves ($T = 1.8s, H = 0.16m, kH/2 = 0.1$) is reproduced by both *foamStar-SWENSE* and *foamStar*.

Comparison of the accuracy

During the simulations, the wave forces and free surface elevations are recorded during 7 periods. The time history is transformed to the frequency domain. The first and second harmonic amplitudes are extracted and compared. The amplitudes of wave force are normalized with $ak\rho g\nabla$, where $a = H/2$ is the amplitude of the waves, k the wave number and ∇ the displacement volume of the buoy at the designed draft. The free surface elevations are normalized by a . The results are shown in Tab. 15. The relative differences compared with the experimental data is given in percentage form.

Table 15: CALM buoy test case: Comparison between CFD results and experimental data for the regular wave case

Harmonic Amplitudes	$F_x^{(1)}$	$F_x^{(2)}$	$F_z^{(1)}$	$F_z^{(2)}$	$\eta_1^{(1)}$	$\eta_1^{(2)}$	$\eta_2^{(1)}$	$\eta_2^{(2)}$	$\eta_3^{(1)}$	$\eta_3^{(2)}$	
Experiment	1.390	0.170	1.180	0.015	1.220	0.065	1.210	0.040	1.040	0.035	
foamStar	x80	1.359	0.168	1.098	0.010	1.195	0.060	1.180	0.036	1.002	0.045
	(2.58M)	-2.23%	-1.18%	-6.95%	-33.33%	-2.05%	-7.69%	-2.48%	-10.00%	-3.65%	28.57%
	x40	1.328	0.165	1.075	0.011	1.172	0.057	1.164	0.035	0.983	0.041
	(1.47M)	-4.46%	-2.94%	-8.90%	-26.67%	-3.93%	-12.31%	-3.80%	-12.50%	-5.48%	17.14%
	x20	1.202	0.130	1.018	0.017	1.063	0.057	1.057	0.037	0.924	0.039
	(1.28M)	-13.53%	-23.53%	-13.73%	13.33%	-12.87%	-12.31%	-12.64%	-7.50%	-11.15%	11.43%
foamStar-SWENSE	x80	1.383	0.182	1.152	0.014	1.211	0.060	1.198	0.032	1.035	0.051
	(2.58M)	-0.50%	7.06%	-2.37%	-6.67%	-0.74%	-7.69%	-0.99%	-20.00%	-0.48%	45.71%
	x40	1.376	0.181	1.144	0.012	1.208	0.060	1.195	0.032	1.028	0.051
	(1.47M)	-1.01%	6.47%	-3.05%	-20.00%	-0.98%	-7.69%	-1.24%	-20.00%	-1.15%	45.71%
	x20	1.360	0.183	1.134	0.011	1.199	0.059	1.185	0.039	1.020	0.051
	(1.28M)	-2.16%	7.65%	-3.90%	-26.67%	-1.72%	-9.23%	-2.07%	-2.50%	-1.92%	45.71%
Cylind.	1.357	0.181	1.146	0.020	1.187	0.065	1.176	0.031	1.010	0.050	
	(0.72M)	-2.37%	6.47%	-2.88%	33.33%	-2.70%	0.00%	-2.81%	-22.50%	-2.88%	42.86%

To analyze the results, let us focus first on the first harmonic amplitudes of the horizontal wave force:

- x80 (total cells 2.58M): The results of both solvers are in good agreement with the experiment. *foamStar* gives slightly smaller predictions of the first harmonic amplitudes. The *foamStar-SWENSE* result has a better agreement with the experiment.
- x40 (total cells 1.47M): *foamStar-SWENSE* is able to predict the wave force and elevation correctly with an accuracy of 1%. Whereas, this difference is about 4% for *foamStar*.
- x20 (total cells 1.28M): This discretization is known to be too coarse to simulate waves in conventional NS solvers. The coarse mesh causes excessive numerical diffusion and damps the incident waves. For this reason, *foamStar* predicts a force 13.5% smaller. However, *foamStar-SWENSE*'s relative error is still within 3%.
- Cylindrical (total cells 0.72M): This configuration is optimal for the SWENSE method. With only 0.72 million cells, the results of *foamStar-SWENSE* is almost as accurate as the result of *foamStar* with x80 mesh (2.58 million cells).

Comparison of the computational cost

The computational times required by *foamStar-SWENSE* and *foamStar* are tested, the results are listed in Tab. 16. The computation is done with 24 2.5GHz processors. The wall-clock time per wave period is compared.

Table 16 first suggests that the computational time on the same mesh is similar for the two solvers. This information suggests that the extra terms in the governing equations of SWENSE and the associated calculations do not influence much the total computational time.

Table 16: CALM buoy test case: Computational time comparison of *foamStar* and *foamStar-SWENSE*

Mesh	Number of cells	Computational time per wave period (360 timesteps)	
		<i>foamStar</i>	<i>foamStar-SWENSE</i>
Cylind.	0.72 M	-	2417s
x20	1.28 M	6030s	6031s
x40	1.47 M	6808s	6782s
x80	2.58 M	10364s	9939s

Secondly, *foamStar-SWENSE* shows a clear advantage when considering the computational time at the same accuracy. *foamStar-SWENSE* with the x20 or the cylindrical mesh obtains the same level of accuracy as *foamStar* using the x80 mesh. A speed-up between 1.71 (with x20) to 4.28 (with the cylindrical mesh) is achieved compare with *foamStar* using x80 mesh. This speed-up would be even much larger in multi-directional wave cases. In that scenario, the mesh for *foamStar* could not be defined with a less resolved transversal direction, while *foamStar-SWENSE* can still use the cylindrical mesh. Besides, in an irregular wave case, the mesh of *foamStar* has to be defined by the smallest wave length of the irregular wave spectrum and thus contains even more cells than the present case.

Please note that the SWENSE method is not designed to reduce computational cost by allowing larger timesteps. The same CFL criterion should be set for both solvers since they convect variables with the same total velocity field. In this test, the same timestep (1/360 wave period) is used for all the simulations. The maximum CFL number is about 30 (near the refinement zone of the skirt) and the CFL number in the farfield is about 0.2. These values are coherent with other similar simulations [70].

Comparison of the flow details

To ensure the correctness of the simulation, especially to validate the result of *foamStar-SWENSE* on the coarse mesh, the flow details of the simulation are compared. Figures 27 and 28 plot the velocity field, Q-criteria and the pressure fields obtained by *foamStar* and *foamStar-SWENSE* with x80 and x20, respectively. Good agreement is observed.

5.3.4 Irregular waves

This section aims to validate the SWENSE method in irregular wave cases. The force on the buoy is recorded and compared with the experimental data.

Incident waves

The irregular waves are unidirectional, generated according to a JONSWAP spectrum ($T_p = 2.0s$, $H_s = 0.12m$, $\gamma = 3$). The motion of the wave-maker is provided to the *HOS-NWT* to calculate the incident wave field in the entire wave tank and then interpolated to the CFD mesh defined near the structure.

Computational Domain

The computational domain of this test case is illustrated by Fig. 29. The cylindrical mesh is the same one in the regular wave case with the same relaxation zone. The simulation thus reproduces only the first 100 s of the experiment.

Results

The comparison of the simulation results and the experimental data, represented by the horizontal and vertical wave forces time history, is shown in Fig. 30. A very good agreement is observed. At the beginning

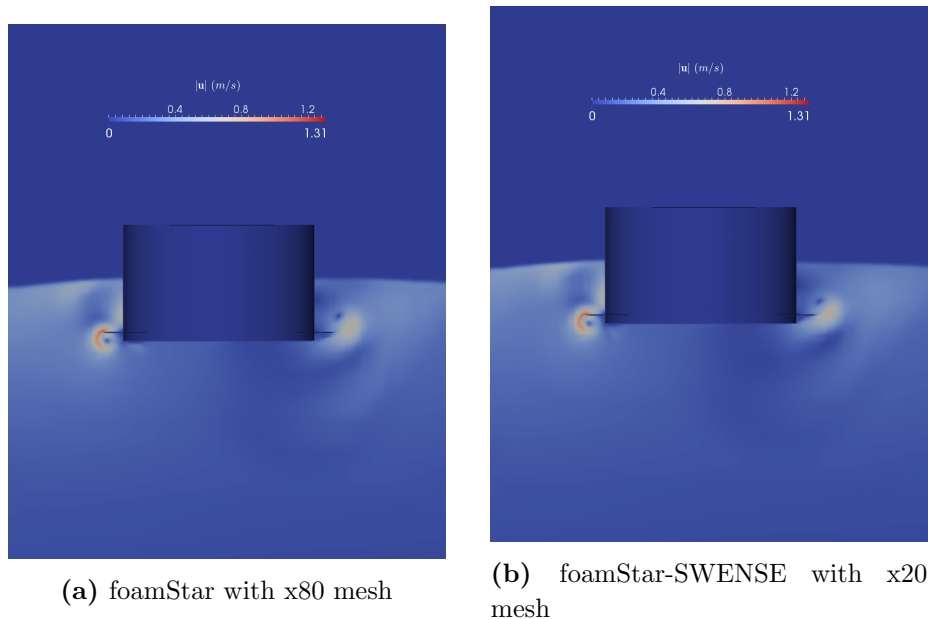


Figure 27: Comparison of the velocity field in the water when a wave crest passes the buoy

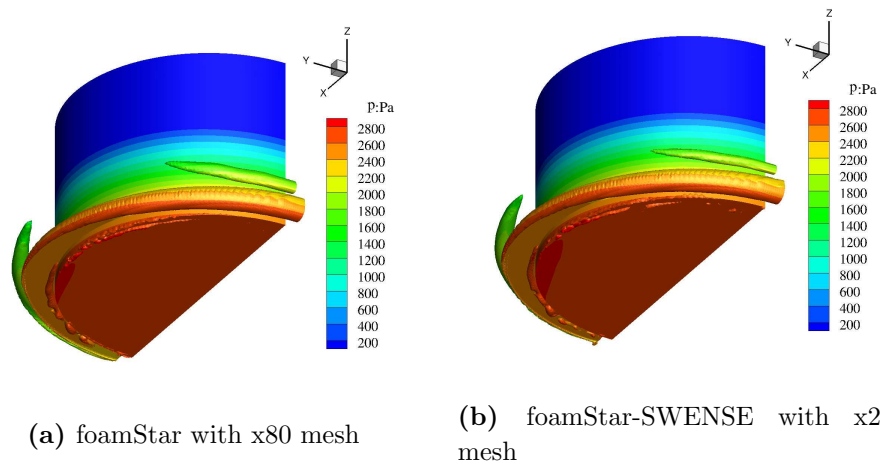


Figure 28: CALM buoy test case: Comparison of the iso-surfaces of $Q = 50$ and pressure field when a wave crest passes the buoy [53]. Reprinted with permission, copyright Elsevier[®].

of the simulation where the wave-front does not reach the structure, the wave forces remain zero. After the wave arrival, the simulated wave force curves are very close to the experimental data during most of the simulation time. Both the amplitudes and the phases are in good agreement.

Figure 31 gives a focused view between $t = 61s$ and $t = 64s$, where a large wave group reaches the buoy. The time histories of forces, both in the horizontal and the vertical direction, are in good agreement with the experimental data. Note that the simulation results have a peak value slightly larger than the experimental data. It may be due to the overprediction of wave velocity in the crest related to the HOS method [26].

Flow details near the structure are provided in Fig. 32. The free surface (approximated by the contour of VOF field $\alpha = 0.5$) is plotted, colored by the free surface elevation η . The time interval between each figure is 0.1s. Violent free surface deformations are observed near the structure. At $t = 62.95s$, a large

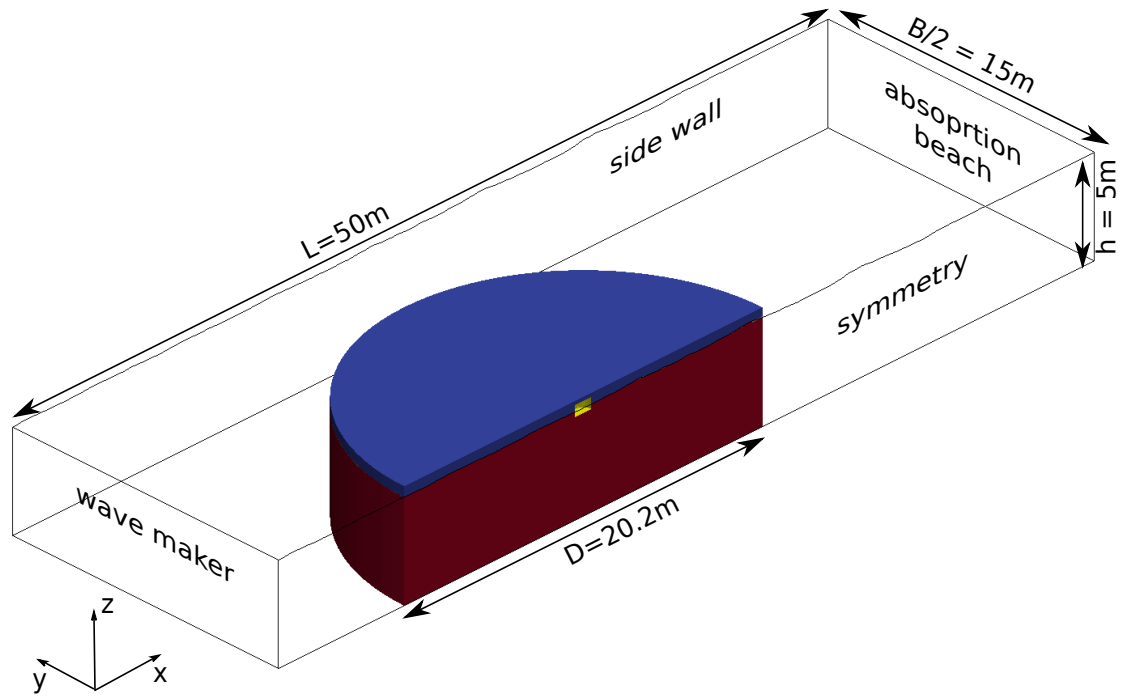
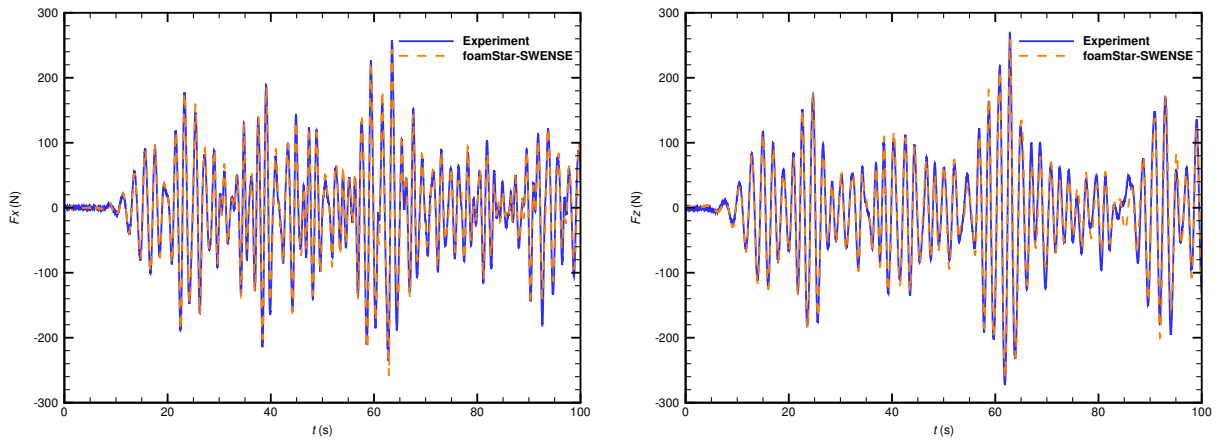


Figure 29: CALM buoy test case: Computational domain of CALM buoy in irregular waves.



(a) Horizontal wave force

(b) Vertical wave force

Figure 30: CALM buoy test case: wave forces in irregular waves

runup occurs on the structure, corresponding to the peak in the time history of force. The wave breaking at $t = 63.1s$ demonstrates that the present two-phase SWENSE method is able to treat violent free surface deformation.

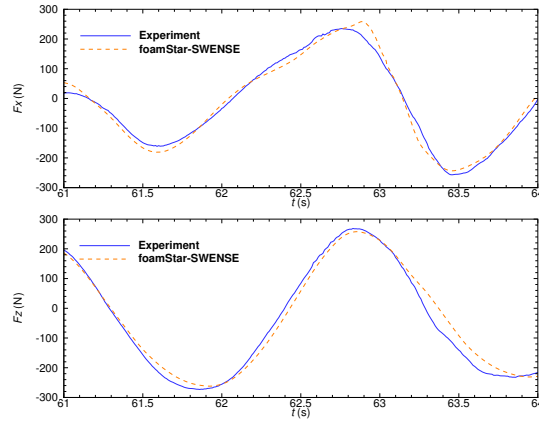


Figure 31: CALM buoy test case: wave forces in irregular waves (zoomed)

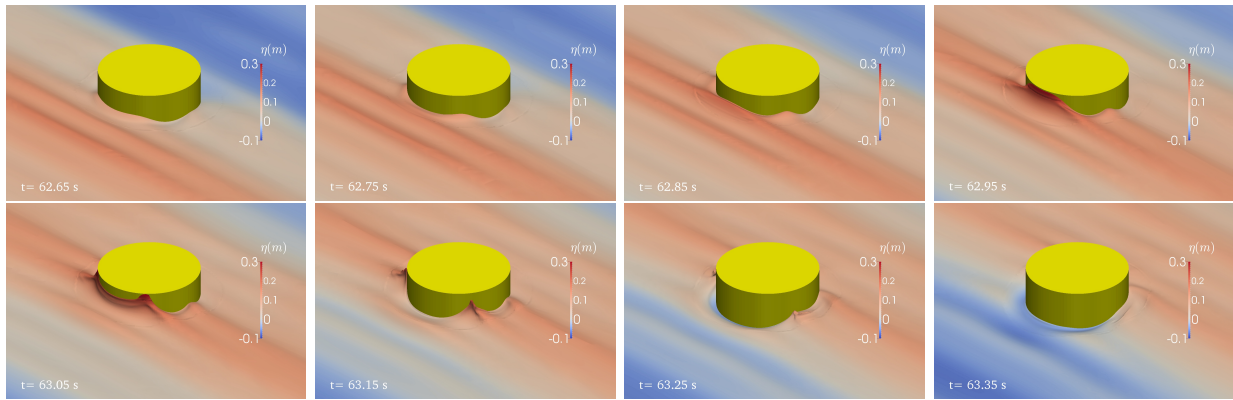


Figure 32: CALM buoy test case: The free surface (contour of $\alpha = 0.5$) close to the buoy when a large wave group passes

6 Conclusion

In this paper, the two-phase Spectral Wave Explicit Navier-Stokes Equations (SWENSE) method is proposed to improve the efficiency and accuracy of two-phase CFD solvers when they are applied to wave-dominated phenomena. The method decomposes the total problem into an incident wave part and a complementary part. Only the latter part is solved by the CFD solver, while the incident wave solution is provided by nonlinear wave models based on spectral representation.

The governing equations of the complementary part are established from the two-phase Navier-Stokes equations and a modified version of Euler equations for incident waves. The proposed equations are mathematically equivalent to the two-phase Navier-Stokes equations and are able to keep the accuracy of the incident waves with coarse CFD mesh. The solution of the Euler equations is obtained by two spectral PT models, assuming the velocity field is irrotational: the stream function wave theory for regular waves and the HOS method for arbitrary waves in open sea or in an experimental wave tank. The definition zone and the solution of the Euler equations are extended in the air-phase.

An accurate and efficient interpolation method to map the results of HOS wave models onto the CFD

mesh is proposed. The method is able to reduce divergence error of the interpolated velocity field to meet the CFD solver’s need without reprojection. This interpolation method is made available for the public through an open source project *Grid2Grid* [19].

An implementation example is shown with a customized solver, *foamStar-SWENSE* in OpenFOAM, based on an existing Navier-Stokes solver *foamStar*. The implementation is straight-forward requiring only the modification of the governing equations.

The method is validated with three validation and application cases: The incident wave propagation cases prove the essential advantage of the SWENSE method, i.e., allowing the use of coarse CFD mesh to simulate incident waves: the SWENSE solver can use a grid 4 times more coarse than that of the NS solver (in each dimension) to achieve the same accuracy for the application of incident waves. The high-order wave loads on a vertical cylinder calculated with the SWENSE method agree well with the reference experimental and numerical results. The convergence study shows a second-order convergence behavior of the solver, which is consistent with the numerical schemes used in OpenFOAM. Note that if only the dominant order is considered, the coarsest discretization can provide a good prediction with an error of less than 10%. This property is useful to give a fast estimation of the wave force, when the absolute accuracy is not very important, *e.g.*, in the early design stage. The CALM buoy case validates the accuracy of the method with complex flow phenomena and reveals its advantage in efficiency. When comparing the computational time to achieve a same level of accuracy, the proposed two-phase SWENSE method achieves a speed-up between 1.71 to 4.28 compared with an NS solver on the regular wave case. This speed-up would be much larger in an irregular and/or multi-directional situation.

The present work contains the following limitations:

- The incident waves are limited to non-breaking waves propagating at a constant water depth, due to the spectral wave models used here. Such limitations can be overcome in future developments by using advanced spectral wave models allowing wave breaking [78, 79] and variable water-depth [39].
- The method is unsuitable for problems with important air effects. In the present work, the extended air velocity is nonphysical. Special treatments should be designed to correct this extended air field, when the air effects cannot be neglected.
- The present implementation approximates the interface position in the simplest manner (VOF contour $\alpha = 0.5$). In the future, VOF methods with interface reconstruction (such as PLIC [77]) or sharp interface methods (such as Level-Set [80]) can be considered to improve the accuracy.
- The validation cases are limited to the calculation of the wave force on a fixed structure. However, in most marine and offshore applications, a moving structure is of interest. The next step of the work is to extend the two-phase SWENSE method to deal with moving structures.

Most of the numerical implementation is based on open source codes: OpenFOAM [8], *HOS-Ocean* [3], *HOS-NWT* [2], and *Grid2Grid* [1]. The reader is encouraged to reproduce this work and go beyond the present limitations.

Acknowledgements

This work has been performed in the framework of the Chaire Hydrodynamique et Structure Marines CENTRALE NANTES - BUREAU VERITAS. The first author acknowledges China Scholarship Council (CSC) for the financial support for his Ph.D. study. The authors are indebted to Dr. Vukčević, Prof. Jasak from

University of Zagreb and Dr. Deng from Ecole Centrale Nantes for their help in this work. Three anonymous reviewers are also gratefully acknowledged.

Appendix A Problem with the direct subtraction of the Euler Equations

This section shows the numerical difficulties appearing when the Euler equation is directly subtracted from the two-phase Navier-Stokes Equations.

Recalling the NS momentum equation for two-phase incompressible fluid (Eqn. 6)

$$\frac{\partial \mathbf{u}}{\partial t} + \mathbf{u} \cdot \nabla \mathbf{u} = -\frac{\nabla p}{\rho} + \mathbf{g} + \frac{\nabla \cdot ((\mu + \mu_t) (\nabla \mathbf{u} + \nabla \mathbf{u}^T))}{\rho}$$

The perfect fluid Euler momentum equation (Eqn. 9) reads:

$$\frac{\partial \mathbf{u}_I}{\partial t} + \mathbf{u}_I \cdot \nabla \mathbf{u}_I = -\frac{\nabla p_I}{\rho_I} + \mathbf{g}$$

To demonstrate the challenge, we now subtract the two equations directly and simplify the viscous terms as in Eqn. (21). We obtain:

$$\frac{\partial \mathbf{u}_C}{\partial t} + \mathbf{u}_C \cdot \nabla \mathbf{u}_C + \mathbf{u}_C \cdot \nabla \mathbf{u}_I + \mathbf{u}_I \cdot \nabla \mathbf{u}_C = -\frac{\nabla p_C}{\rho} + \frac{\nabla p_I}{\rho_I} - \frac{\nabla p_I}{\rho} + \frac{\nabla \cdot ((\mu + \mu_t) (\nabla \mathbf{u}_C + \nabla \mathbf{u}_C^T))}{\rho} \quad (63)$$

The underlined terms are canceled out in the water since $\rho = \rho_I$. However, these terms have non-zero values in the air phase. They behave as source terms and affect the numerical stability.

Appendix B Comparison of Level-Set and Volume of Fluid method

The decomposed Level-Set (DLS) method [87] and the standard Volume of Fluid method (VOF) are compared here with a pure convection case. The transporting velocity is the incident wave velocity obtained from PT (same as in Sect. 5.1). The computational domain, boundary conditions are also the same as in Sect. 5.1. Five meshes are used: Three are the same as in Sect. 5.1: fine ($\Delta x, \Delta z = \lambda/200, H/40$), medium ($\Delta x, \Delta z = \lambda/100, H/20$), coarse ($\Delta x, \Delta z = \lambda/50, H/10$), two coarser meshes are in addition: ($\Delta x, \Delta z = \lambda/25, H/5$) and ($\Delta x, \Delta z = \lambda/15, H/3$).

The measurement and postprocessing procedures are the same as in Sect. 5.1. Figure 33 shows the first harmonic amplitudes of the free surface elevation (nondimensionalised by the target value). The DLS method shows no advantages against the VOF method. The VOF method creates only 1% error with the coarsest mesh, ($\Delta x, \Delta z = \lambda/15, H/3$), suggesting the VOF method can work together with the SWENSE method to reduce the mesh.

References

- [1] Grid2Grid: HOS Wrapper for C++/fortran CFD solvers. <https://github.com/LHEEA/Grid2Grid>. Accessed: 2018-08-15.

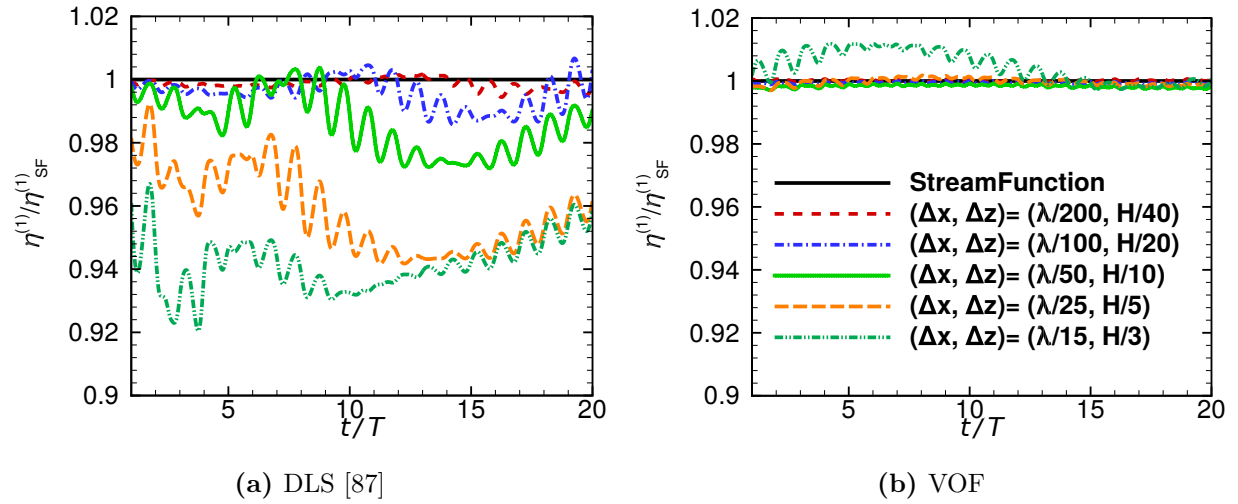


Figure 33: First harmonic amplitude of free surface elevation obtained with the passive transport of the decomposed Level-Set (DLS) and the Volume-of-Fluid (VOF) field by the incident wave velocity field. The amplitude is normalised with the target value.

- [2] Numerical Wave Tank based on High-Order Spectral method . <https://github.com/LHEEA/HOS-NWT>, . Accessed: 2018-08-15.
- [3] High-Order Spectral method for oceanic simulations. <https://github.com/LHEEA/HOS-ocean>, . Accessed: 2018-08-15.
- [4] CN-Stream: Computation of nonlinear regular ocean waves using stream function. <https://github.com/LHEEA/CN-Stream>. Accessed: 2019-02-13.
- [5] OpenFOAM guide/Reconstruction. https://openfoamwiki.net/index.php/OpenFOAM_guide/Reconstruction, . Accessed: 2019-02-13.
- [6] CFD online: fvc::reconstruct algorithm. <https://www.cfd-online.com/Forums/openfoam-programming-development/77943-fvc-reconstruct-algorithm.html>, . Accessed: 2019-08-14.
- [7] OpenFOAM User Guide. <https://www.openfoam.com/>, . Accessed: 2018-08-15.
- [8] About OpenFOAM . <https://www.openfoam.com/>, . Accessed: 2018-08-15.
- [9] S. Abadie, D. Morichon, S. Grilli, and S. Glockner. Numerical simulation of waves generated by landslides using a multiple-fluid Navier–Stokes model. *Coastal engineering*, 57(9):779–794, 2010.
- [10] A. Albadawi, D. Donoghue, A. Robinson, D. Murray, and Y. Delauré. On the assessment of a vof based compressive interface capturing scheme for the analysis of bubble impact on and bounce from a flat horizontal surface. *International journal of multiphase flow*, 65:82–97, 2014.
- [11] A. Babarit and G. Delhommeau. Theoretical and numerical aspects of the open source BEM solver NEMOH. In *11th European Wave and Tidal Energy Conference (EWTEC2015)*, 2015.
- [12] K. Bai and R. Yeung. Numerical solutions to free-surface flow problems. In *Symposium on Naval Hydrodynamics, 10th, Proceedings, Pap and Discuss, Cambridge, Massachusetts, 1974.*, 1974.

- [13] H. B. Bingham and H. Zhang. On the accuracy of finite-difference solutions for nonlinear water waves. *Journal of Engineering Mathematics*, 58(1-4):211–228, 2007.
- [14] E. Campana, A. Di Mascio, P. Esposito, and F. Lalli. Viscous-inviscid coupling in free surface ship flows. *International Journal for Numerical Methods in Fluids*, 21(9):699–722, 1995.
- [15] P. M. Carrica, R. V. Wilson, and F. Stern. Unsteady RANS simulation of the ship forward speed diffraction problem. *Computers & Fluids*, 35(6):545 – 570, 2006.
- [16] H.-C. Chen and S.-K. Lee. RANS/Laplace calculations of nonlinear waves induced by surface-piercing bodies. *Journal of engineering mechanics*, 125(11):1231–1242, 1999.
- [17] L. Chen, J. Zang, A. Hillis, G. Morgan, and A. Plummer. Numerical investigation of wavestructure interaction using OpenFOAM. *Ocean Engineering*, 88:91 – 109, 2014.
- [18] Y. Choi, B. Bouscasse, S. Seng, G. Ducrozet, L. Gentaz, and P. Ferrant. Generation of regular and irregular waves in Navier-Stokes CFD solvers by matching with nonlinear potential wave solution at the boundary. In *Proceedings of the ASME 2018 37th International Conference on Ocean, Offshore and Arctic Engineering*, June 2018.
- [19] Y. Choi, M. Gouin, G. Ducrozet, B. Bouscasse, and P. Ferrant. Grid2Grid : HOS Wrapper Program for CFD solvers. *ArXiv e-prints*, Dec. 2018.
- [20] E. D. Christensen, H. Bredmose, and E. A. Hansen. Transfer of Boussinesq waves to a Navier-Stokes solver: Application to wave loads on an offshore wind turbine foundation. In *ASME 2009 28th International Conference on Ocean, Offshore and Arctic Engineering*, pages 917–926. American Society of Mechanical Engineers, 2009.
- [21] G. Colicchio, M. Greco, and O. M. Faltinsen. A BEM-Level Set domain-decomposition strategy for nonlinear and fragmented interfacial flows. *International journal for numerical methods in engineering*, 67(10):1385–1419, 2006.
- [22] R. G. Dean and R. A. Dalrymple. *Water wave mechanics for engineers and scientists*, volume 2. World Scientific Publishing Company, 1991.
- [23] S. S. Deshpande, L. Anumolu, and M. F. Trujillo. Evaluating the performance of the two-phase flow solver interFoam. *Computational science & discovery*, 5(1):014016, 2012.
- [24] D. G. Dommermuth. The laminar interactions of a pair of vortex tubes with a free surface. *Journal of Fluid Mechanics*, 246:91–115, 1993.
- [25] D. G. Dommermuth and D. K. Yue. A high-order spectral method for the study of nonlinear gravity waves. *Journal of Fluid Mechanics*, 184:267–288, 1987.
- [26] G. Ducrozet. *Modélisation des processus non-linéaires de génération et de propagation d’états de mer par une approche spectrale*. PhD thesis, Université de Nantes; Ecole Centrale de Nantes (ECN), 2007.
- [27] G. Ducrozet, F. Bonnefoy, D. Le Touzé, and P. Ferrant. A modified high-order spectral method for wavemaker modeling in a numerical wave tank. *European Journal of Mechanics-B/Fluids*, 34:19–34, 2012.
- [28] G. Ducrozet, F. Bonnefoy, D. L. Touz, and P. Ferrant. HOS-ocean: Open-source solver for nonlinear waves in open ocean based on High-Order Spectral method. *Computer Physics Communications*, 203: 245 – 254, 2016.

- [29] G. Ducrozet, F. Bonnefoy, and Y. Perignon. Applicability and limitations of highly non-linear potential flow solvers in the context of water waves. *Ocean Engineering*, 142:233–244, 2017.
- [30] G. Ducrozet, F. Bonnefoy, B. Bouscasse, M. Gouin, and P. Ferrant. CN-Stream: Open-source library for nonlinear regular waves using stream function theory. *Computer Physics Communications*, in prep.
- [31] L. Eça and M. Hoekstra. A procedure for the estimation of the numerical uncertainty of CFD calculations based on grid refinement studies. *Journal of Computational Physics*, 262:104–130, 2014.
- [32] D. O. Edmund, K. J. Maki, and R. F. Beck. A velocity-decomposition formulation for the incompressible navier–stokes equations. *Computational Mechanics*, 52(3):669–680, 2013.
- [33] O. M. Faltinsen, J. N. Newman, and T. Vinje. Nonlinear wave loads on a slender vertical cylinder. *Journal of Fluid Mechanics*, 289:179–198, 1995.
- [34] P. Ferrant. Computation of higher order diffraction effects using a fully nonlinear simulation method. *Proc. 11th International Workshop on Water Waves and Floating Bodies, Hamburg*, 1996.
- [35] P. Ferrant. Fully nonlinear interactions of long-crested wave packets with a three dimensional body. In *Proc. 22nd ONR Symposium on Naval Hydrodynamics*, pages 403–415, 1998.
- [36] P. Ferrant, L. Gentaz, B. Alessandrini, and D. Le Touzé. A potential/RANSE approach for regular water wave diffraction about 2-D structures. *Ship Technology Research*, 50(4):165–171, 2003.
- [37] P. Ferrant, L. Gentaz, B. Alessandrini, R. Luquet, C. Monroy, G. Ducrozet, E. Jacquin, and A. Drouet. Fully nonlinear potential/RANSE simulation of wave interaction with ships and marine structures. In *ASME 2008 27th International Conference on Offshore Mechanics and Arctic Engineering*, pages 379–387. American Society of Mechanical Engineers, 2008.
- [38] J. H. Ferziger and M. Peric. *Computational methods for fluid dynamics*. Springer Science & Business Media, 2012.
- [39] M. Gouin, G. Ducrozet, and P. Ferrant. Development and validation of a non-linear spectral model for water waves over variable depth. *European Journal of Mechanics-B/Fluids*, 57:115–128, 2016.
- [40] S. Grilli, R. Gilbert, P. Lubin, S. Vincent, D. Astruc, D. Legendre, M. Duval, O. Kimmoun, H. Branger, D. Devrard, et al. Numerical modeling and experiments for solitary wave shoaling and breaking over a sloping beach. In *14th International offshore and polar engineering conference*. International Society of Offshore and Polar Engineers, 2004.
- [41] S. Guignard, S. T. Grilli, R. Marcer, V. Rey, et al. Computation of shoaling and breaking waves in nearshore areas by the coupling of BEM and VOF methods. In *The Ninth International Offshore and Polar Engineering Conference*. International Society of Offshore and Polar Engineers, 1999.
- [42] P. Higuera, J. Lara, and I. Losada. Realistic wave generation and active wave absorption for Navier-Stokes models Application to OpenFOAM. *Coastal Engineering*, 71:102–118, 01 2013.
- [43] C. W. Hirt and B. D. Nichols. Volume of fluid (VOF) method for the dynamics of free boundaries. *Journal of Computational Physics*, 39(1):201 – 225, 1981.
- [44] M. Huseby and J. Grue. An experimental investigation of higher-harmonic wave forces on a vertical cylinder. *Journal of fluid Mechanics*, 414:75–103, 2000.
- [45] A. Iafrati, A. Di Mascio, and E. Campana. A level set technique applied to unsteady free surface flows. *International Journal for Numerical Methods in Fluids*, 35(3):281–297, 2001.

- [46] ITTC. *Practical guidelines for ship CFD applications ITTC Recommended Procedures and Guidelines 7.5-03-02-03*, 2014.
- [47] N. G. Jacobsen, D. R. Fuhrman, and J. Fredsøe. A Wave Generation Toolbox for the Open-Source CFD Library: OpenFOAM®. *International Journal for Numerical Methods in Fluids*, 70(9):1073–1088, 2012.
- [48] H. Jasak, V. Vukčević, I. Gatin, and I. Lalović. CFD validation and grid sensitivity studies of full scale ship self propulsion. *International Journal of Naval Architecture and Ocean Engineering*, 11(1):33–43, 2019.
- [49] K. Kim, A. I. Sirviente, and R. F. Beck. The complementary RANS equations for the simulation of viscous flows. *International journal for numerical methods in fluids*, 48(2):199–229, 2005.
- [50] C. Lachaume, B. Biausser, P. Fraunié, S. T. Grilli, S. Guignard, et al. Modeling of breaking and post-breaking waves on slopes by coupling of BEM and VOF methods. In *The Thirteenth International Offshore and Polar Engineering Conference*. International Society of Offshore and Polar Engineers, 2003.
- [51] B. Lalanne, L. R. Villegas, S. Tanguy, and F. Risso. On the computation of viscous terms for incompressible two-phase flows with level set/ghost fluid method. *Journal of Computational Physics*, 301: 289–307, 2015.
- [52] Z. Li, L. Gentaz, G. Ducrozet, and P. Ferrant. Calculation of high-order wave loads on a vertical circular cylinder using the swense method. In *Proc. 32th International Workshop on Water Waves and Floating Bodies (IWWF, Dalian, China, April 2017)*, 2017.
- [53] Z. Li, G. Deng, P. Queutey, B. Bouscasse, G. Ducrozet, L. Gentaz, D. Le Touzé, and P. Ferrant. Comparison of wave modeling methods in CFD solvers for ocean engineering applications. *Ocean Engineering*, 188:106237, 2019.
- [54] F. Liu. A thorough description of how wall functions are implemented in OpenFOAM. *Proceedings of CFD with OpenSource Software*, pages 1–33, 2016.
- [55] X. Lu, D. D. J. Chandar, Y. Chen, and J. Lou. An overlapping domain decomposition based near-far field coupling method for wave structure interaction simulations. *Coastal Engineering*, 126:37–50, 2017.
- [56] R. Luquet, P. Ferrant, B. Alessandrini, G. Ducrozet, and L. Gentaz. Simulation of a TLP in waves using the swense scheme. In *The Seventeenth International Offshore and Polar Engineering Conference*. International Society of Offshore and Polar Engineers, 2007.
- [57] Q. Ma and S. Yan. Quasi ALE finite element method for nonlinear water waves. *Journal of computational physics*, 212(1):52–72, 2006.
- [58] Š. Malenica and B. Molin. Third-harmonic wave diffraction by a vertical cylinder. *Journal of Fluid Mechanics*, 302:203–229, 1995.
- [59] A. D. Mascio, R. Broglia, and R. Muscari. On the application of the single-phase level set method to naval hydrodynamic flows. *Computers & Fluids*, 36(5):868 – 886, 2007.
- [60] A. Mehmood, D. I. Graham, K. Langfeld, and D. M. Greaves. OpenFOAM Finite Volume Method Implementation of a Fully Nonlinear Potential Flow Model for Simulating Wave-Structure Interactions. In *The Twenty-fifth International Ocean and Polar Engineering Conference*. International Society of Offshore and Polar Engineers, 2015.

- [61] F. R. Menter. Two-equation eddy-viscosity turbulence models for engineering applications. *AIAA journal*, 32(8):1598–1605, 1994.
- [62] C. Monroy. *Simulation numérique de l'interaction houle-structure en fluide visqueux par décomposition fonctionnelle*. PhD thesis, Ecole Centrale de Nantes (ECN), 2010.
- [63] C. Monroy and S. Seng. Time-stepping schemes for seakeeping in OpenFOAM. In *Proceedings of the 10th International Workshop on Ship and Marine Hydrodynamics*, November 2017.
- [64] C. Monroy, S. Seng, and S. Malenica. Développements et validation de l'outil CFD OpenFOAM pour le calcul de tenue à la mer. In *Proceedings of the 15th Journées de l'Hydrodynamique*, November 2016.
- [65] F. Moukalled, L. Mangani, and M. Darwish. *The Finite Volume Method in Computational Fluid Dynamics An Advanced Introduction with OpenFOAM and Matlab*. Springer, 2016.
- [66] J. Newman and C.-H. Lee. Boundary-element methods in offshore structure analysis. *Journal of Offshore Mechanics and Arctic Engineering*, 124(2):81–89, 2002.
- [67] OpenFOAM. OpenFOAM: User guide v1906, 2019. URL <https://www.openfoam.com/documentation/guides/latest/doc/guide-applications-solvers-pimple.html>.
- [68] B. T. Paulsen, H. Bredmose, and H. B. Bingham. An efficient domain decomposition strategy for wave loads on surface piercing circular cylinders. *Coastal Engineering*, 86:57–76, 2014.
- [69] P. Queutey, E. Guilmineau, M. Visonneau, J. Wackers, and G. Deng. RANS and Hybrid RANS-LES simulations around the Japan Bulk Carrier of the Tokyo 2015 CFD Workshop. In *19th Numerical Towing Tank Symposium (NuTTS 2016)*, 10 2016.
- [70] E. Ransley, S. Yan, S. A. Brown, T. Mai, D. Graham, Q. Ma, P.-H. Musiedlak, A. P. Engsig-Karup, C. Eskilsson, Q. Li, et al. A blind comparative study of focused wave interactions with a fixed FPSO-like structure (CCP-WSI Blind Test Series 1). *International Journal of Offshore and Polar Engineering*, 29(02):113–127, 2019.
- [71] G. Reliquet. *Simulation numérique de l'interaction houle/carène par couplage d'une méthode spectrale HOS avec un algorithme de capture d'interface*. PhD thesis, Ecole Centrale de Nantes, 2013.
- [72] G. Reliquet, A. Drouet, P.-E. Guillerm, E. Jacquin, L. Gentaz, and P. Ferrant. Simulation of wave-body interaction using a single-phase level set function in the SWENSE method. In *ASME 2013 32nd International Conference on Ocean, Offshore and Arctic Engineering*. American Society of Mechanical Engineers, 2013.
- [73] M. M. Rienecker and J. D. Fenton. A Fourier approximation method for steady water waves. *Journal of Fluid Mechanics*, 104:119–137, 1981.
- [74] W. J. Rosemurgy, R. F. Beck, and K. J. Maki. A velocity decomposition formulation for 2D steady incompressible lifting problems. *European Journal of Mechanics-B/Fluids*, 58:70–84, 2016.
- [75] Rousset, J.-M. and Ferrant, P. Model tests for Principia R&D. Technical Report CTR1 - JIP Calm Buoy 2, Laboratoire de Mécanique des Fluides de l'Ecole Centrale de Nantes (UMR CNRS 6598), 2005.
- [76] H. Rusche. *Computational fluid dynamics of dispersed two-phase flows at high phase fractions*. PhD thesis, Imperial College London (University of London), 2003.
- [77] R. Scardovelli and S. Zaleski. Direct numerical simulation of free-surface and interfacial flow. *Annual review of fluid mechanics*, 31(1):567–603, 1999.

- [78] B. R. Seiffert and G. Ducrozet. Simulation of breaking waves using the high-order spectral method with laboratory experiments: wave-breaking energy dissipation. *Ocean Dynamics*, 68(1):65–89, 2018.
- [79] B. R. Seiffert, G. Ducrozet, and F. Bonnefoy. Simulation of breaking waves using the high-order spectral method with laboratory experiments: Wave-breaking onset. *Ocean Modelling*, 119:94–104, 2017.
- [80] J. A. Sethian and P. Smereka. Level set methods for fluid interfaces. *Annual review of fluid mechanics*, 35(1):341–372, 2003.
- [81] Y. L. Shao and O. M. Faltinsen. A harmonic polynomial cell (HPC) method for 3D Laplace equation with application in marine hydrodynamics. *Journal of Computational Physics*, 274:312 – 332, 2014.
- [82] M. Siddiqui, M. Greco, G. Colicchio, and O. M. Faltinsen. Validation of damaged ship hydrodynamics by a Domain Decomposition Approach using the Harmonic Polynomial Cell method and OpenFOAM. In *33th International Workshop on Water Waves and Floating Bodies*, 2018.
- [83] F. Stern, J. Yang, Z. Wang, H. Sadat-Hosseini, M. Mousaviraad, S. Bhushan, and T. Xing. Computational ship hydrodynamics: nowadays and way forward. *International Shipbuilding Progress*, 60(1-4): 3–105, 2013.
- [84] G. G. Stokes. *On the Theory of Oscillatory Waves*, volume 1 of *Cambridge Library Collection - Mathematics*, page 197229. Cambridge University Press, 2009.
- [85] O. Ubbink and R. Issa. A method for capturing sharp fluid interfaces on arbitrary meshes. *Journal of computational physics*, 153(1):26–50, 1999.
- [86] H. K. Versteeg and W. Malalasekera. *An introduction to computational fluid dynamics: the Finite Volume method*. Pearson Education, 2007.
- [87] V. Vukčević, H. Jasak, and Š. Malenica. Decomposition model for naval hydrodynamic applications, Part I: Computational method. *Ocean Engineering*, 121:37–46, 2016.
- [88] B. J. West, K. A. Brueckner, R. S. Janda, D. M. Milder, and R. L. Milton. A new numerical method for surface hydrodynamics. *Journal of Geophysical Research: Oceans*, 92(C11):11803–11824, 1987.
- [89] Y. Zhang, M. Peszynska, and S. Yim. Coupling of viscous and potential flow models with free surface for near and far field wave propagation. *Int J Numer Anal Model*, 4(3):256–82, 2013.